buildings

MDPI

Article

Enhanced Modified Compression Field Theory-Based Shear Capacity Prediction of Ultra-High-Performance Concrete (UHPC) Beams with Steel Fibers and Stirrups

Tadesse G. Wakjira

Department of Civil and Environmental Engineering, Kennesaw State University, 1100 South Marietta Pkwy SE, Marietta, GA 30060, USA; twakjira@kennesaw.edu

Abstract

Most design provisions for the shear capacity of ultra-high-performance concrete (UHPC) beams require a measured tensile input, such as the localization tensile stress or a residual flexural strength, that is unavailable before the mix is finalized. This study proposes an Enhanced Modified Compression Field Theory (EMCFT) that predicts the shear capacity from inputs available at the design stage, with the fiber volume fraction (ρ_f), the fiber aspect ratio (l_f/d_f), and the compressive strength (f'_c) in place of a measured tensile property. The principal tensile stress is decomposed into a composite tension stiffening baseline and a separable fiber bridging term that depends on the fiber reinforcing index $\psi_f = \rho_f \cdot l_f/d_f$. The fiber coefficients are determined from independent pullout mechanics as $\alpha_f = 0.19$ and $\alpha_p = 135$, with α_p matched to the crack width at 50% fiber stress reduction. Consequently, the model contains only two fitted parameters, namely the composite baseline coefficient $\alpha_m = 1.085$ (95% confidence interval [0.988, 1.181]) and an I-section flange participation factor $k = 0.307$ (95% confidence interval [0.184, 0.470]). For 45 beams, the leave-one-out cross-validated mean experimental-to-predicted ratio is 1.007, with a coefficient of variation of 9.3%.

Keywords: ultra-high-performance concrete; UHPC; shear capacity; modified compression field theory; steel fibers; fiber bridging

1. Introduction

Ultra-high-performance concrete (UHPC) is an advanced cementitious composite characterized by a high compressive strength and a high toughness [1–3]. In addition, UHPC exhibits a sustained post-cracking tensile strength through the incorporation of steel fibers [4–6]. The combination of a dense matrix, a very low water-to-binder ratio, and a high dosage of steel fibers produces a material that exhibits strain-hardening behavior in direct tension, superior durability, and energy absorption capacity that far exceed those of conventional and high-strength concrete [1,7,8]. These properties have led to a rapid expansion of UHPC applications over the past decade, particularly in bridge girders, precast segmental elements, bridge deck overlays [9], and field-cast joints between precast deck panels [10]. For UHPC columns, the confinement [11], the seismic behavior with high-strength steel reinforcement [12], and the buckling of full-scale slender members [13] have been investigated. Numerical models, performance-based seismic design procedures, and seismic vulnerability and resilience assessments have been developed for UHPC bridge piers, columns, and bridges [14–16]. Other applications include shear walls [17] and the

Check for updates

Academic Editor: Piti Sukontasukkul

Received: 20 September 2026
Revised: 18 October 2026
Accepted: 22 October 2026
Published: 29 October 2026

Copyright: © 2026 by the author. Licensee MDPI, Basel, Switzerland. This article is an open access article distributed under the terms and conditions of the Creative Commons Attribution (CC BY) license.

strengthening of shear walls [18]. UHPC jackets and precast UHPC plates have been investigated for the seismic retrofitting of columns [19–21]. In these applications, the reduced member dimensions can produce substantial savings in material volume and structural weight [22,23].

Steel fibers govern the post-cracking response of UHPC, and the effects of fiber content, fiber shape, and fiber–matrix bond have been investigated at the material and member levels. Wu et al. [24] examined the effects of steel fiber content and shape on the mechanical properties of UHPC, and Yoo et al. [25] investigated the effect of fiber content on the mechanical and fracture properties of ultra-high-performance fiber-reinforced cementitious composites. Wille and Naaman [26] showed that the pullout resistance of high-strength steel fibers embedded in UHPC depends strongly on the fiber shape, with substantially higher bond strengths for deformed fibers than for straight fibers. In conventional fiber-reinforced concrete, Minelli and Plizzari [27] showed that a fiber volume fraction below 0.7% can increase the shear strength and ductility of beams without transverse reinforcement. Pekgökgöz and Avcil [28] reported that a steel fiber volume fraction of 1% increased the energy dissipation capacity of beam–column joints under reversed cyclic loading by 10% to 12% and limited the damage to the concrete through the increase in shear strength. For UHPC beams, Pourbaba et al. [29] observed much higher shear strength and ductility than in conventional concrete beams. Lim and Hong [30] found that steel fibers substantially improved the shear resistance of UHPC beams with stirrups and that the stirrups had a synergistic effect on ductility, with shear strengths above the predictions of the American Concrete Institute (ACI) 318-14 even when the stirrup spacing exceeded the code limit. Zagon et al. [31] examined the shear behavior of I-shaped UHPC beams reinforced with steel fibers. These studies show that the shear resistance of fiber-reinforced members depends on fiber content, fiber geometry, and the interaction between fibers and stirrups.

The prediction of shear capacity remains one of the most challenging aspects of UHPC structural design, primarily since the shear transfer mechanisms in UHPC differ fundamentally from those in conventional concrete [32,33]. In normal-strength concrete, diagonal tension resistance is provided by aggregate interlock along the crack surface and dowel action of the longitudinal reinforcement, and both mechanisms diminish rapidly as cracks widen. Extensive experimental research has been conducted over the past two decades to characterize the shear behavior of UHPC beams. Baby et al. [34] tested eleven I-shaped UHPC girders with prestressed or mild steel longitudinal reinforcement and demonstrated that the inclusion of steel fibers substantially increased the shear capacity, with the fiber orientation at the crack face exerting a strong influence on the measured capacity. Voo et al. [35] tested prestressed UHPC beams without stirrups, with the shear span-to-depth ratio and the quantity and type of steel fibers as test variables. In these beams, the UHPC was designed to carry the full shear force. Yavaş et al. [36] tested fifteen UHPC beams without shear reinforcement and showed that the addition of 1.5% of 13 mm straight steel fibers changed the failure mode from shear to flexure. More recently, Sun et al. [37] tested eleven prestressed UHPC beams and found that the shear behavior was primarily governed by the shear span-to-depth ratio, with secondary influences from the stirrup ratio and the prestressing force.

Despite the substantial experimental evidence, the prediction of shear capacity in UHPC beams that contain both fibers and stirrups remains insufficiently addressed. Most experimental programs have focused on beams without stirrups [35], prestressed members [34,37], or specific cross-sectional geometries, and the interaction between the fiber bridging mechanism and the transverse steel reinforcement has attracted comparatively less attention. Database studies interpreted with Shapley additive explanations identify the cross-sectional geometry and the shear span-to-depth ratio as the dominant parameters,

followed by the fiber content [38,39]. However, a mechanics-based model that represents the fiber bridging stress separately from the tension stiffening of the composite within a compression field formulation has not been reported. The shear design formulation of El-Helou and Graybeal [40] for strain-hardening fiber-reinforced concrete beams forms the basis of the design provisions of the Federal Highway Administration (FHWA) [41]. In these provisions, the shear resistance is expressed as $V_{\mathrm{UHPC}} = \gamma_u \cdot f_{t,\mathrm{loc}} \cdot b_v \cdot d_v \cdot \cot\theta$, where b_v is the effective web width, equal to b_w for the beams considered here, $f_{t,\mathrm{loc}}$ is the localization tensile stress obtained from experimental direct tension tests, and θ is the crack angle determined through the Modified Compression Field Theory (MCFT). Machine learning approaches have been explored [38,42,43], but these models lack the mechanical transparency necessary for code adoption.

Existing models have two main limitations. First, the FHWA model requires the localization tensile stress $f_{t,\mathrm{loc}}$ measured in direct tension tests on the specific UHPC mix [41], and most other analytical approaches require a tensile property measured in direct tension or prism bending tests. This measurement requirement limits the applicability of these models in preliminary design and parametric studies. Second, the shear contribution of UHPC is typically expressed as a single term that lumps two physically distinct mechanisms, namely, the tension stiffening between cracks and the fiber bridging across the crack. This lumped representation obscures the relative contributions of tension stiffening and fiber bridging and prevents a rational decomposition of the shear resistance. Such a decomposition is required for the extension of design equations to new fiber types and volume fractions without full recalibration.

The MCFT, developed by Vecchio and Collins [44] and simplified by Bentz et al. [45], provides a rigorous mechanics-based framework that satisfies equilibrium, compatibility, and constitutive relationships simultaneously. The MCFT has been extensively validated for normal-strength and high-strength concrete [45] and forms the basis of the shear provisions in the Canadian Standards Association (CSA) standard A23.3 [46,47]. In addition, the American Association of State Highway and Transportation Officials (AASHTO) load and resistance factor design (LRFD) Bridge Design Specifications and the FHWA UHPC provisions [41] are based on the MCFT. Previous extensions of the MCFT framework have been proposed for beams strengthened with fabric reinforced cementitious matrix [48,49] and composite members strengthened with UHPC [50]. Diab and Ferche [51] proposed an MCFT-based shear strength model for UHPC members incorporating fiber orientation and cross-sectional shape effects, evaluated on a database of 534 specimens. However, their formulation requires the direct tension characteristics of the specific UHPC mix, and these characteristics were reported for only 106 of their 534 tests and otherwise had to be estimated by a machine learning model from the mix composition. Few mechanics-based models address monolithic UHPC beams containing both dispersed steel fibers and stirrups. Apart from the UHPC provision of the Precast/Prestressed Concrete Institute (PCI-UHPC) [52], with a residual tensile strength independent of the fiber properties, none of these models can be applied with inputs available at the design stage.

To address the aforementioned research gaps, this study proposes an Enhanced Modified Compression Field Theory (EMCFT) for UHPC beams with steel fibers and stirrups that requires no tensile test on the specific mix. The model decomposes the principal tensile stress into a composite tension stiffening baseline and a separable fiber bridging term, $f_{1,f} = \alpha_f \sqrt{f'_c}\, \rho_{f,\mathrm{eff}}\, (l_f/d_f)/(1+\alpha_p \varepsilon_x)$, that depends on the fiber reinforcing index $\psi_f = \rho_f \cdot l_f/d_f$, where ρ_f is the fiber volume fraction and l_f/d_f is the fiber aspect ratio. The fiber bridging term is expressed as a function of ρ_f, l_f/d_f, and the compressive strength f'_c, all available at the design stage. As a result, the localization tensile stress $f_{t,\mathrm{loc}}$ required by the FHWA provisions [41] is not needed. In addition, an identifiability analysis shows that, on a database

where every specimen contains fibers, the beam tests determine the fiber coefficient α_f only in combination with the baseline coefficient α_m. Therefore, the fiber coefficients are fixed from independent pullout mechanics, and the model retains an explicit and physically bounded fiber term with only two fitted parameters, namely α_m and the I-section flange participation factor k. The model is validated by leave-one-out cross-validation and cross-validation with complete source studies withheld. Furthermore, the predictive performance is compared on the same 45 beams with the PCI-UHPC provision, the FHWA and Association Française de Génie Civil (AFGC) provisions with estimated tensile inputs, and the simplified MCFT (SMCFT). Finally, a reliability-based resistance factor is calibrated under the LRFD framework of ACI 318-19 [53]. The proposed model allows the shear capacity of UHPC beams to be evaluated at the preliminary design stage, before mix-specific tensile tests are available.

2. Methodology

2.1. Theoretical Framework

The MCFT, developed by Vecchio and Collins [44], models cracked reinforced concrete as a continuous material governed simultaneously by equilibrium, compatibility, and stress–strain relationships. Unlike truss-analogy models that assume a fixed 45° crack angle and neglect the tensile capacity of cracked concrete, the MCFT determines both the angle of inclination of the diagonal compressive stresses (θ) and the average principal tensile stress (f_1) as part of the solution. This formulation allows the theory to capture the experimentally observed variation of crack angles with loading intensity and reinforcement ratios [44]. In addition, simplified compression field formulations have been developed for the shear design of reinforced concrete beams strengthened with fabric reinforced cementitious matrix [48,49].

At a cracked section of a reinforced concrete element subjected to shear, the MCFT vertical equilibrium requires that the applied shear force (V) be carried by the combined action of the principal tensile stress on the crack face and the transverse reinforcement crossing the crack. For a beam web element located away from concentrated loads and reactions, the applied transverse clamping stress is negligible ($f_y = 0$). Therefore, the transverse direction is internally self-equilibrated, with the concrete carrying a vertical compression that balances the stirrup tension ($f_{cy} = -\rho_{sv} f_{sv}$), and the applied shear is carried entirely by the inclined tensile stress and the stirrups. This equilibrium condition is given by [44,45]:

$$V = f_1 \cdot b_w \cdot d_v \cdot \cot\theta + \rho_{sv} \cdot f_{sv} \cdot b_w \cdot d_v \cdot \cot\theta \quad (1)$$

where b_w is the web width, d_v is the effective shear depth, θ is the angle of diagonal compression measured from the longitudinal axis, ρ_{sv} is the transverse reinforcement ratio ($A_v/b_w s$, where A_v is the stirrup area and s is the stirrup spacing), and f_{sv} is the stress in the transverse reinforcement, taken as the yield strength of the stirrups. The $\cot\theta$ factor arises from the projection of the stress normal to the inclined crack plane into the vertical direction. For a crack inclined at an angle θ, the area of the crack plane is $b_w \cdot d_v / \sin\theta$, and the vertical component of the normal stress is $f_1 \cdot \cos\theta$. The product of the crack plane area and the vertical stress component is the vertical shear contribution $f_1 \cdot b_w \cdot d_v \cdot \cot\theta$ (Figure 1a).

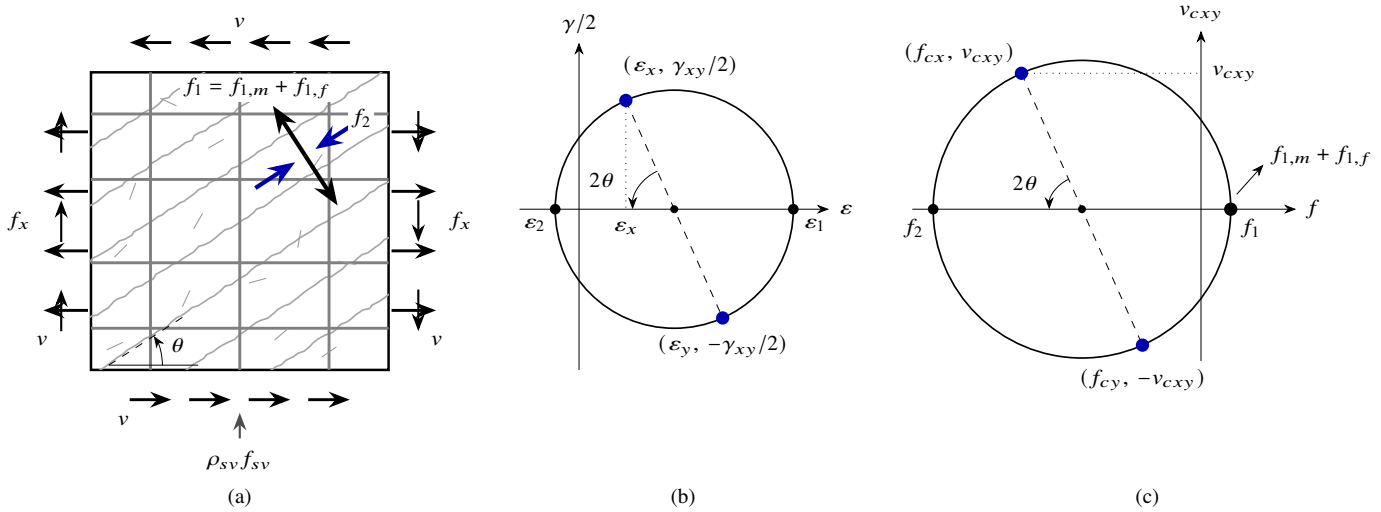


Figure 1. MCFT-based equilibrium of a UHPC beam element within the shear span, showing (**a**) the equilibrium of forces on the cracked element with the principal tensile stress decomposed into the composite baseline and fiber bridging contributions, (**b**) the Mohr's circle for average strains, and (**c**) the Mohr's circle for average stresses.

2.2. Extension to UHPC with Steel Fibers

In conventional concrete, the principal tensile stress f_1 is attributed primarily to tension stiffening between cracks, limited at the crack by the shear transferred through aggregate interlock [44,45]. UHPC reinforced with discontinuous steel fibers introduces an additional tensile resistance mechanism, with fibers bridging the diagonal crack and sustaining tensile stress normal to the crack face at crack widths well beyond those at the exhaustion of the baseline tension stiffening. The magnitude of the fiber contribution relative to the composite baseline is quantified in Section 3.5. To incorporate this mechanism within the MCFT framework, the principal tensile stress f_1 is decomposed into two contributions (Figure 1), as given by:

$$f_1 = f_{1,m} + f_{1,f} \tag{2}$$

where $f_{1,m}$ is the composite tension stiffening baseline stress and $f_{1,f}$ is the separable fiber bridging contribution that depends on the fiber reinforcing index ψ_f. The two terms act at different locations and scales. The baseline stress $f_{1,m}$ represents tension stiffening in the intact material between cracks, whereas $f_{1,f}$ represents the stress transmitted across the crack face by fibers that are progressively pulled out as the crack opens. Since these mechanisms are physically independent, the two stresses are taken as additive within the MCFT equilibrium framework. The beam tests determine the total stress f_1, and the split between the two terms is fixed from pullout mechanics (Section 3.2). Therefore, $f_{1,m}$ represents a composite property of fibrous UHPC instead of a fiber-free matrix property. When Equation (2) is substituted into Equation (1), the total shear resistance is expressed as the sum of three mechanistically distinct components, as given by:

$$V = V_c + V_f + V_s \leq V_{\max} \tag{3}$$

where each component is given by:

$$V_c = f_{1,m} \cdot b_w \cdot d_v \cdot \cot\theta \tag{4}$$

$$V_f = f_{1,f} \cdot b_w \cdot d_v \cdot \cot\theta \tag{5}$$

$$V_s = \rho_{sv} \cdot f_{sv} \cdot b_w \cdot d_v \cdot \cot\theta \tag{6}$$

Here, V_c is the composite baseline shear contribution from tension stiffening, V_f is the fiber shear contribution from fiber bridging across the crack, and V_s is the stirrup contribution. All three shear mechanisms share the $\cot\theta$ multiplier. For V_c and V_f, the $\cot\theta$ multiplier arises from the projection of the tensile stress normal to the inclined crack into the vertical direction, whereas for V_s the multiplier reflects the number of stirrups, $d_v \cot\theta/s$, that cross the inclined crack (Figure 1a).

The upper bound $V_{\max}$ in Equation (3) represents the diagonal strut crushing capacity. In the original MCFT, this limit is governed by the softened compressive strength of the cracked concrete. From the Mohr's circle equilibrium (Figure 1c), the shear stress is related to the principal stresses as $v = (f_1 + f_2)/(\tan\theta + \cot\theta)$, and the maximum diagonal compressive stress f_2 is limited by the softened compressive strength [44,45], as given by:

$$f_{c2,\max} = \frac{f'_c}{0.8 + 170\,\varepsilon_1} \le f'_c \tag{7}$$

where ε_1 is the principal tensile strain. Therefore, when the small f_1 contribution in the Mohr relation is conservatively neglected, the diagonal strut crushing capacity is given by:

$$V_{\max} = f_{c2,\max} \cdot b_w \cdot d_v \cdot \sin\theta \cdot \cos\theta \tag{8}$$

The principal tensile strain ε_1 is estimated from the longitudinal strain as $\varepsilon_1 \approx \varepsilon_x(1 + \cot^2\theta)$, following the Mohr's circle compatibility condition (Figure 1b) with the small ε_2 term neglected. Bentz et al. [45] evaluated this expression at typical failure strains, found that the maximum shear stress ranges from $0.28f'_c$ to $0.32f'_c$ depending on ε_x, and adopted $0.25f'_c$ as a conservative simplification for the SMCFT. The proposed model retains the full MCFT expression of Equations (7) and (8) for accuracy.

2.3. Constitutive Equations

2.3.1. Composite Tension Stiffening Baseline

The composite baseline term $f_{1,m}$ represents the tension stiffening effect that develops between cracks in fibrous UHPC. It is adapted from the strain-dependent form of Vecchio and Collins [44] as simplified by Bentz et al. [45]. Since α_m is calibrated on a database where every specimen contains steel fibers, α_m necessarily absorbs the average fiber contribution at the lowest fiber content of the database and represents a composite (fibrous UHPC) quantity instead of a fiber-free matrix property. The marginal effect of the fiber reinforcing index ψ_f above that baseline is captured separately by the explicit term $f_{1,f}$, as described in the following subsection. The composite baseline stress is given by:

$$f_{1,m} = \frac{\alpha_m \sqrt{f'_c}}{1 + 1500\,\varepsilon_x} \tag{9}$$

where ε_x is the longitudinal strain at mid-depth and α_m is the composite tension stiffening baseline coefficient. In the original MCFT, the principal tensile stress after cracking is expressed as $f_1 = f_{cr}/\left(1 + \sqrt{200\,\varepsilon_1}\right)$ with $f_{cr} \approx 0.33\sqrt{f'_c}$ [44] (Collins et al. [54] later suggested replacing 200 by 500 for larger elements), and the expression corresponds to an f_1 coefficient of 0.33 in the SMCFT formulation of Bentz et al. [45]. The calibrated value of $\alpha_m = 1.085$ is substantially larger than the conventional concrete coefficient of 0.33. The rationale that UHPC should have a reduced coefficient since it lacks coarse aggregate conflates two distinct mechanisms. Aggregate interlock transfers shear parallel to the crack, whereas $f_{1,m}$ is a tensile stress normal to it. The post-cracking tensile capacity of UHPC is far higher than that of conventional concrete, consistent with the cracking stress $f_{cr} = 0.6\sqrt{f'_c}$ adopted in Equation (15).

2.3.2. Fiber Bridging Stress

The fiber bridging contribution represents the tensile stress transmitted across the diagonal crack by steel fibers that bridge the crack faces. This term is derived from the composite pullout mechanics framework developed by Li [55] and Naaman [56]. The fiber bridging stress is given by:

$$f_{1,f} = \frac{\alpha_f \sqrt{f'_c} \cdot \rho_{f,\text{eff}} \cdot (l_f/d_f)}{1 + \alpha_p \, \varepsilon_x}, \qquad \rho_{f,\text{eff}} = \min\left(\rho_f, 0.02\right) \tag{10}$$

where ρ_f is the fiber volume fraction (decimal), l_f is the fiber length (mm), d_f is the fiber diameter (mm), α_f is the fiber bridging coefficient, and α_p is the fiber pullout degradation parameter.

The numerator of Equation (10) is grounded in established composite mechanics. When randomly oriented steel fibers cross a crack, the average bridging stress carried by the fibers across the crack is $\sigma_{fb} = \eta_o \cdot \eta_l \cdot \eta_s \cdot \tau_b \cdot \rho_f \cdot (l_f/d_f)$, where η_o is the fiber orientation efficiency factor (that accounts for the three-dimensional random distribution of fibers relative to the crack plane), η_l is the length efficiency factor (that accounts for the variable embedment lengths on either side of the crack), η_s is the fiber group efficiency factor (that accounts for the interaction between closely spaced fibers), and τ_b is the average fiber–matrix interfacial bond stress. For UHPC, the interfacial bond stress is assumed to scale approximately with $\sqrt{f'_c}$ due to the dense microstructure and strong fiber–matrix bond. The coefficient α_f is obtained when σ_{fb} is normalized by $\sqrt{f'_c}$ and all efficiency factors are combined into a single coefficient fixed from pullout mechanics. The product $\rho_f \cdot (l_f/d_f)$, commonly referred to as the fiber reinforcing index (ψ_f), is a well-established parameter that governs the post-cracking tensile performance of fiber-reinforced concrete [56].

Here, $\rho_{f,\text{eff}} = \min(\rho_f, 0.02)$ is the effective fiber volume fraction. This limit reflects the experimentally observed behavior that pullout bond strength in UHPC increases with fiber dosage up to approximately $\rho_f = 0.02$ (2%) and declines at higher dosages [25]. Accordingly, dosages above 2% are not credited with proportionally greater bridging stress. The limit is imposed as a physical bound and introduces no fitted parameter. The strain-dependent denominator $(1 + \alpha_p \, \varepsilon_x)$ captures the progressive degradation of fiber bridging stress as diagonal cracks widen under increased shear distress. This degradation is physically caused by the gradual pullout and debonding of fibers as crack openings increase. The functional form is analogous to the tension stiffening degradation in Equation (9), but with a degradation rate approximately 11 times slower ($\alpha_p = 135$ versus 1500 for the baseline term). This large difference reflects the experimentally observed behavior that steel fibers maintain substantial bridging capacity at crack widths of 1–2 mm [57], well beyond the crack widths of 0.05–0.1 mm associated with the loss of most of the tensile stress of the matrix [58]. The degradation of the fiber contribution with increasing crack width is well established in the literature. The diverse embedment model [59] and its simplified form [58] derive the bridging stress as an explicit function of the crack width (w). Similarly, the AFGC $\sigma(w)$ approach [60,61] defines the bridging stress as a function of w. The proposed formulation evaluates the degradation in strain space through the SMCFT variable ε_x and eliminates the need for an explicit crack width computation or an iterative solution on w. The correspondence between ε_x and the crack width used to fix α_p is described in Section 3.2.

In I-section beams, part of the compression flange participates in the transfer of shear stresses. To account for this effect, an effective web width b_{eff} is introduced for I-sections,

and b_{eff} reduces to b_w for rectangular sections and T-sections. The effective web width is given by:

$$b_{\text{eff}} = b_w + k\left(b_f - b_w\right)\frac{t_f}{d_v} \tag{11}$$

where b_f is the flange width, t_f is the flange thickness, and k is a calibrated flange participation factor. The effective width b_{eff} replaces b_w in the computation of the shear contributions V_c and V_f and the diagonal strut crushing capacity $V_{\max}$, since these terms represent shear resisting mechanisms with flange participation. However, b_{eff} is not used in the longitudinal reinforcement area $A_s = \rho_l b_w d$, the stirrup contribution $V_s = \rho_{sv} f_{sv} b_w d_v \cot\theta$, or the tension chord area $A_{ct} = 0.5\, b_w d_v$. Since both ρ_l and ρ_{sv} are defined against the web width in the source database, the use of b_{eff} for these quantities would attribute reinforcement area that the specimens do not contain. Similarly, A_{ct} is a flexural tension quantity, and applying a shear effective width to it would conflate two distinct mechanisms.

2.3.3. Crack Inclination Angle

The angle of inclination of the diagonal compression strut is determined from the SMCFT [45], as given by:

$$\theta = (29 + 7000\,\varepsilon_x)\left(0.88 + \frac{s_{xe}}{2500}\right) \le 75^\circ \tag{12}$$

where s_{xe} is the equivalent crack spacing parameter (mm) that accounts for the size effect in shear. For members with transverse reinforcement, Bentz et al. [45] noted that the diagonal crack spacing is typically less than 300 mm and recommended that s_{xe} be taken as 300 mm in both the tensile stress factor and the crack angle expressions. When s_{xe} is taken as 300 mm, the size effect factor $(0.88 + 300/2500)$ equals 1.00, and Equation (12) reduces to Equation (13).

$$\theta = 29 + 7000\,\varepsilon_x \qquad (25^\circ \le \theta \le 50^\circ) \tag{13}$$

This simplified form is adopted in the proposed model since all beams in the database contain transverse reinforcement. The limits $25^\circ \le \theta \le 50^\circ$ applied to Equation (13) are a practical range consistent with comparable provisions, and the 75° bound of Equation (12) applies to the full expression. For comparison, the PCI-UHPC provision [52] bounds the strain in its crack angle expression $\theta = 29^\circ + 3500\,\varepsilon_s$ to $-0.4 \times 10^{-3} \le \varepsilon_s \le 6.0 \times 10^{-3}$, corresponding to 27.6°–50.0°. Equation (12) is the product of a strain factor and a size factor chosen to match the predictions of the full MCFT. For 102 panel tests, Bentz et al. [45] reported a mean test-to-prediction ratio of 1.11 with a coefficient of variation (CoV) of 13.0% for the simplified expressions, compared with 1.01 (CoV of 12.2%) for the full MCFT.

2.3.4. Longitudinal Strain at Mid-Depth

The longitudinal strain at mid-depth of the beam is computed from the mid-depth strain expression of the SMCFT [45,47], as adopted in CSA A23.3 [46]. The expression is augmented with a UHPC tensile force term based on the FHWA provisions [41]. The SMCFT expression contains the factor of two in the denominator and is the form used to derive the crack angle relation $\theta = 29 + 7000\,\varepsilon_x$. Since the localization tensile stress $f_{t,\text{loc}}$ used by FHWA is unavailable at the design stage, the cracking stress $f_{cr} = 0.6\sqrt{f'_c}$ is substituted in that term, with the FHWA variability reduction factor γ_u carried over. The term $\gamma_u \cdot f_{cr} \cdot A_{ct}$ in the numerator of Equation (14) represents the tensile force sustained by the UHPC and reduces the strain demand on the longitudinal reinforcement compared to conventional concrete, where cracked concrete carries no tension. This modification is essential for UHPC since ε_x would be overestimated without the tensile contribution of UHPC, leading to an overestimation of θ and consequent underestimation of the shear capacity. The resulting

expression, with the axial force N_u and the vertical prestress component V_p omitted for the members considered here, is given by:

$$\varepsilon_x = \frac{|M_u/d_v| + |V_u| - A_{ps}f_{po} - \gamma_u \cdot f_{cr} \cdot A_{ct}}{2\left(E_s A_s + E_p A_{ps}\right)} \tag{14}$$

where M_u is the moment at the section, V_u is the shear force at the section, A_{ps} is the area of prestressing steel, f_{po} is the stress in the prestressing steel corresponding to the locked-in strain difference between the prestressing steel and the surrounding concrete, and E_p is the elastic modulus of the prestressing steel.

For non-prestressed beams ($A_{ps} = 0$, $V_p = 0$, $N_u = 0$), the moment is evaluated at the AASHTO critical section, one effective shear depth from the support [41], where $M_u = Vd_v$ and $|M_u|/d_v = V$. Therefore, the moment and shear terms in the numerator of Equation (14) reduce to $2V$, and the longitudinal strain is given by:

$$\varepsilon_x = \frac{|M_u|/d_v + |V| - \gamma_u \cdot f_{cr} \cdot A_{ct}}{2\,E_s\,A_s} = \frac{2\,V - \gamma_u \cdot f_{cr} \cdot A_{ct}}{2\,E_s\,A_s} \tag{15}$$

where E_s is the elastic modulus of the longitudinal reinforcement, taken as 200 GPa, $A_s = \rho_l \cdot b_w \cdot d$ is the area of longitudinal tensile reinforcement, $f_{cr} = 0.6\sqrt{f'_c}$ is the cracking stress of UHPC adopted in the proposed model, within the range of $0.55\sqrt{f'_c}$ to $0.69\sqrt{f'_c}$ reported by Graybeal [62], $A_{ct} = 0.5 \cdot b_w \cdot d_v$ is the tension chord concrete area as adopted in the proposed model (the FHWA provisions [41], following AASHTO LRFD, define A_{ct} as the concrete area on the flexural tension side of mid-depth, approximately $b_w h/2$ for rectangular sections, and the smaller web-based definition is used consistently within the calibrated model), and γ_u is the FHWA factor that reduces the UHPC tensile parameters for members where the tensile properties of the placed UHPC are expected to be lower than the qualified values, for instance as a result of unfavorable fiber distribution or orientation [41]. The FHWA provisions require $\gamma_u \leq 1.0$. Diab and Ferche [51] adopted the value $\gamma_u = 0.85$ of the AASHTO guide specification, and the same value is adopted here. FHWA defines γ_u in conjunction with the measured $f_{t,\mathrm{loc}}$, and γ_u is applied here to the f_{cr}-based estimate.

A negative strain from Equation (14) or (15) indicates that the section at mid-depth is under net compression, a condition possible in members with high prestress or when the tensile force $\gamma_u \cdot f_{cr} \cdot A_{ct}$ exceeds $2V$. In this case, the denominator is augmented to include the axial stiffness of the concrete in the tensile zone, as given by:

$$\varepsilon_x = \frac{2\,V - \gamma_u \cdot f_{cr} \cdot A_{ct}}{2(E_s\,A_s + E_c\,A_{ct})} \tag{16}$$

where $E_c = 3840\sqrt{f'_c}$ (MPa) is the elastic modulus of UHPC [62]. The longitudinal strain is limited to the range $-0.0002 \leq \varepsilon_x \leq 0.006$.

2.4. Iterative Solution Procedure

Equations (3)–(15) form a coupled nonlinear system since the shear capacity V depends on ε_x through the crack angle θ and the stress terms $f_{1,m}$ and $f_{1,f}$, while ε_x itself depends on V through Equation (15). This coupling is resolved through a damped fixed-point iteration scheme, with the shear force estimate successively refined until the difference between consecutive estimates falls below a prescribed tolerance. The damped update rule $V^{(n+1)} = 0.5\,V_n^{(n)} + 0.5\,V^{(n)}$, where $V_n^{(n)}$ is the newly computed capacity and $V^{(n)}$ is the previous estimate, prevents oscillatory divergence that can occur with undamped updates when the shear capacity is sensitive to small changes in ε_x. The complete procedure, shown in the flowchart of Figure 2, consists of the following steps.

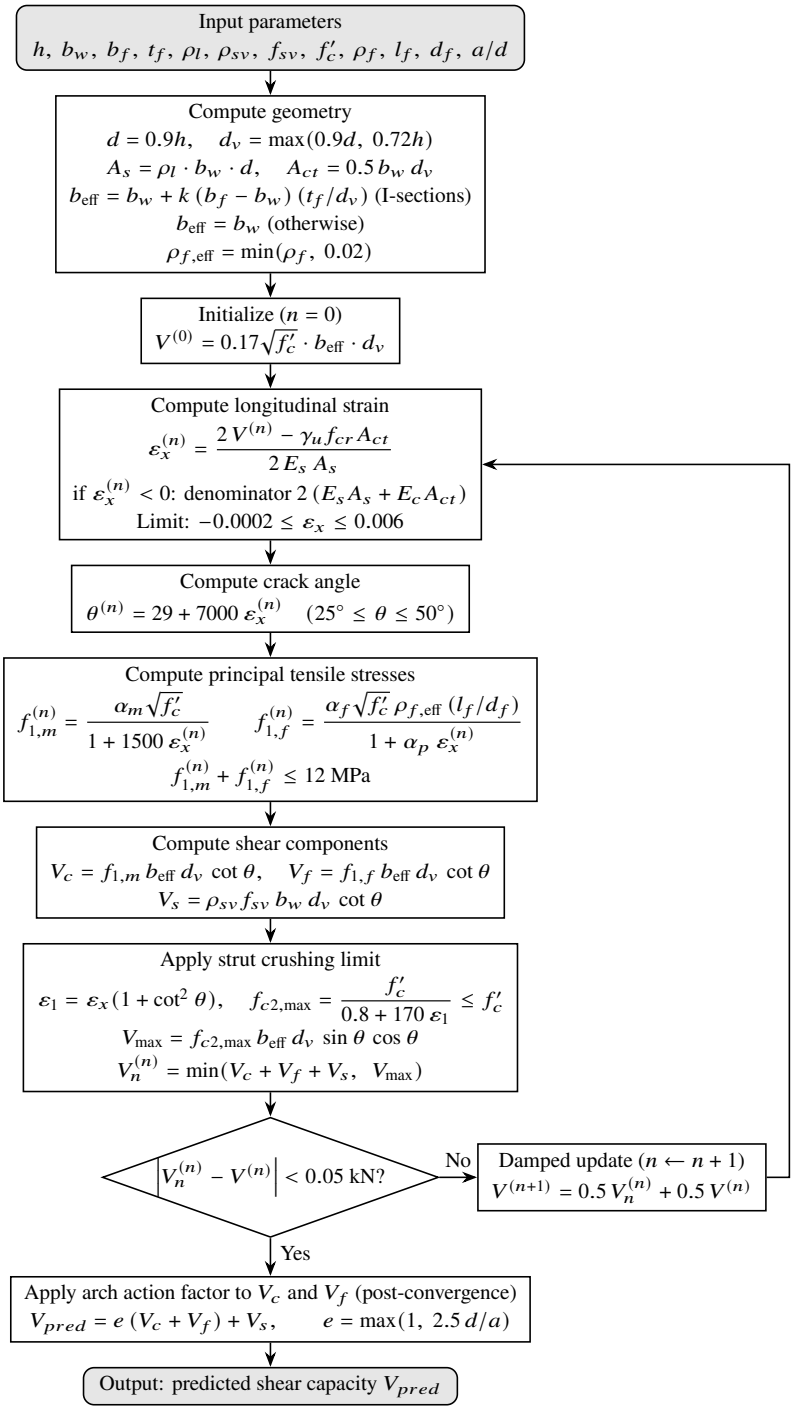


Figure 2. Flowchart of the proposed EMCFT, including the effective width assignment (b_{eff} for V_c and V_f; b_w for V_s), the effective fiber volume fraction $\rho_{f,\text{eff}}$, and the arch action factor applied to V_c and V_f after convergence.

Step 1. Identify the input parameters, namely, h, b_w, b_f and t_f (I-sections), ρ_l, ρ_{sv}, f_{sv}, f'_c, ρ_f, l_f, d_f, and a/d.

Step 2. Determine the effective depth, $d = 0.9h$, the effective shear depth, $d_v = \max(0.9d, 0.72h)$, and the area of longitudinal reinforcement $A_s = \rho_l \cdot b_w \cdot d$.

Step 3. Set the initial shear estimate as $V^{(0)} = 0.17\sqrt{f'_c} \cdot b_{\text{eff}} \cdot d_v$ and the iteration counter as $n = 0$.

Step 4. Evaluate $\varepsilon_x^{(n)}$ from Equation (15) with $V = V^{(n)}$. If $\varepsilon_x^{(n)} < 0$, recompute with the augmented denominator $2(E_s A_s + E_c A_{ct})$. Limit the result to the range $-0.0002 \le \varepsilon_x^{(n)} \le 0.006$.

Step 5. Evaluate $\theta^{(n)}$ from Equation (13) and limit it to $25^\circ \le \theta^{(n)} \le 50^\circ$.

Step 6. Compute the composite baseline $f_{1,m}^{(n)}$ from Equation (9) and the fiber term $f_{1,f}^{(n)}$ from Equation (10), using the effective fiber volume fraction $\rho_{f,\text{eff}}$, with a negative $\varepsilon_x^{(n)}$ taken as zero in both denominators. The composite stress $f_{1,m}^{(n)} + f_{1,f}^{(n)}$ is limited to 12 MPa, close to the upper end of the typical localization tensile stresses of 6.2 to 12.4 MPa given in the FHWA provisions [41].

Step 7. Compute the shear components $V_c^{(n)} = f_{1,m}^{(n)} \cdot b_{\text{eff}} \cdot d_v \cdot \cot\theta^{(n)}$ and $V_f^{(n)} = f_{1,f}^{(n)} \cdot b_{\text{eff}} \cdot d_v \cdot \cot\theta^{(n)}$ using the effective width of Equation (11), and $V_s^{(n)} = \rho_{sv} \cdot f_{sv} \cdot b_w \cdot d_v \cdot \cot\theta^{(n)}$ on the web width, since ρ_{sv} is defined against b_w (Section 2.3).

Step 8. Apply the strut crushing limit. Compute the principal tensile strain as $\varepsilon_1^{(n)} = \varepsilon_x^{(n)}(1 + \cot^2\theta^{(n)})$, evaluate $f_{c2,\max}^{(n)}$ from Equation (7), and compute $V_{\max}^{(n)}$ from Equation (8). Then set $V_n^{(n)} = \min\left(V_c^{(n)} + V_f^{(n)} + V_s^{(n)},\ V_{\max}^{(n)}\right)$.

Step 9. Check convergence. If $|V_n^{(n)} - V^{(n)}| < 0.05$ kN, convergence has been achieved, and $V_{\text{sect}} = V_n^{(n)}$ is taken as the converged sectional shear capacity.

Step 10. If convergence has not been achieved, update the estimate as $V^{(n+1)} = 0.5\,V_n^{(n)} + 0.5\,V^{(n)}$, increment $n \leftarrow n + 1$, and return to Step 4.

Step 11. Apply the arch action factor after convergence. Once the sectional solution V_{sect} has converged, the predicted shear capacity is obtained by applying the arch action factor e to the concrete and fiber contributions, as given by Equation (17).

$$V_{pred} = e\,(V_c + V_f) + V_s, \qquad e = \max(1,\ 2.5\,d/a) \tag{17}$$

This factor accounts for the additional capacity provided by arch action in beams with $a/d < 2.5$ and is applied after the iterative solution has converged. Consistent with the derivation of Zsutty [63] for the concrete contribution, the enhancement is applied to V_c and V_f, and the stirrup contribution V_s, carried by truss action, is not enhanced. The arch action factor does not feed back into the longitudinal strain ε_x, the crack angle θ, or the constitutive stress terms, since arch action represents a resisting mechanism that supplements the sectional capacity instead of a modification of the sectional equilibrium itself.

The coefficients are obtained as described in Section 3.2. The coefficients $\alpha_f = 0.19$ and $\alpha_p = 135$ are fixed from independent pullout mechanics, and $\alpha_m = 1.085$ and the flange participation factor $k = 0.307$ are fitted by Nelder–Mead minimization of the log-space least-squares objective.

2.5. Model Parameters

Table 1 lists the parameters, limits, and numerical settings of the proposed model, with the physical meaning and the origin of each item. Only two parameters are fitted to the beam database, namely the composite baseline coefficient α_m and the flange participation factor k. The fiber coefficients α_f and α_p and the 2% limit on the fiber volume fraction are fixed from fiber pullout mechanics before the calibration. The crack angle relation, size effect factor, and degradation constant of the baseline term are taken from the SMCFT without modification, whereas the cracking stress, variability reduction factor, elastic modulus of UHPC, and arch action factor are taken from the sources listed in Table 1. The strain bounds, crack angle bounds, and tensile stress limit define the domain of validity of the expressions, and the geometric assumptions $d = 0.9h$ and $d_v = \max(0.9d,\ 0.72h)$ are applied uniformly to all beams. The initial estimate, damping factor of 0.5, and convergence tolerance of 0.05 kN are the numerical settings of the solution procedure.

Table 1. Parameters, limits, and numerical settings of the proposed model.

Item	Physical Meaning	Value	Origin
α_m	Composite tension stiffening baseline coefficient, Equation (9)	1.085	Fitted (Section 3.2)
k	Flange participation factor for I-sections, Equation (11)	0.307	Fitted (Section 3.2)
α_f	Fiber bridging coefficient, Equation (10)	0.19	Fixed from pullout mechanics (Section 3.2)
α_p	Fiber pullout degradation parameter, Equation (10)	135	Fixed from the crack width at 50% fiber stress reduction (Section 3.2)
$\rho_{f,\text{eff}}$	Effective fiber volume fraction, Equation (10)	$\min(\rho_f, 0.02)$	Pullout bond tests [25]
1500	Strain degradation constant of the baseline term, Equation (9)	1500	SMCFT [45]
θ	Crack angle, Equations (12) and (13)	$29 + 7000\,\varepsilon_x$, from 25° to 50°	SMCFT [45], with adopted bounds
s_{xe}	Equivalent crack spacing, Equation (12)	300 mm	SMCFT [45]
f_{cr}	Cracking stress of UHPC, Equation (15)	$0.6\sqrt{f'_c}$	Graybeal [62]
γ_u	Tensile variability reduction factor, Equation (15)	0.85	AASHTO guide specification value, as used by Diab and Ferche [51]
A_{ct}	Tension chord area, Equation (15)	$0.5\,b_w d_v$	Adopted
E_s	Elastic modulus of the longitudinal reinforcement, Equation (15)	200 GPa	Adopted
E_c	Elastic modulus of UHPC, Equation (16)	$3840\sqrt{f'_c}$ MPa	Graybeal [62]
ε_x bounds	Strain limits of the solution procedure	−0.0002 to 0.006	Adopted
f_1 limit	Upper bound of the composite tensile stress	12 MPa	Adopted, within the typical range of FHWA [41]
e	Arch action factor applied to $V_c + V_f$, Equation (17)	$\max(1, 2.5\,d/a)$	Zsutty [63]
d, d_v	Effective depth and effective shear depth	$0.9h$, $\max(0.9d, 0.72h)$	Adopted
Iteration	Initial estimate, damping factor, and tolerance	$0.17\sqrt{f'_c}\,b_{\text{eff}}\,d_v$, 0.5, 0.05 kN	Numerical setting

2.6. Evaluation Framework

The predictive accuracy of the model is quantified through the mean, standard deviation, and coefficient of variation of the experimental-to-predicted ratio ($\Theta = V_{exp}/V_{pred}$), the coefficient of determination (R^2), the root mean square error, the mean absolute error, the mean absolute percentage error (MAPE), and the fractions of predictions with $0.85 \le \Theta \le 1.15$ and $0.70 \le \Theta \le 1.30$. The out-of-sample accuracy is evaluated with two cross-validation schemes, and both fitted coefficients are refitted in every fold. In leave-one-out cross-validation (LOOCV), each beam is predicted by the model calibrated on the remaining 44 beams. In leave-one-study-out cross-validation, all beams of one

source study (Section 3.1) are withheld together and predicted by the model calibrated on the other studies. As a result, specimens from one experimental program never appear in both the calibration and test datasets. In addition, the prediction capability is evaluated using the modified Demerit Points Classification (DPC) system [64]. As presented in Table 2, the DPC system classifies each prediction based on the V_{pred}/V_{exp} ratio into five categories, namely extremely dangerous ($V_{pred}/V_{exp} > 2.0$, penalty 10), dangerous ($1.176 \leq V_{pred}/V_{exp} \leq 2.0$, penalty 5), appropriate safety ($0.869 \leq V_{pred}/V_{exp} < 1.176$, penalty 0), conservative ($0.5 \leq V_{pred}/V_{exp} < 0.869$, penalty 1), and extremely conservative ($V_{pred}/V_{exp} < 0.5$, penalty 2), and assigns a cumulative penalty score. A lower total penalty indicates better overall prediction capability in terms of the combined assessment of safety, accuracy, and economy.

Table 2. Modified Demerit Points Classification (DPC) criteria [64].

V_{pred}/V_{exp} Range	Classification	Penalty
>2.0	Extremely dangerous	10
[1.176, 2.0]	Dangerous	5
[0.869, 1.176)	Appropriate safety	0
[0.5, 0.869)	Conservative	1
<0.5	Extremely conservative	2

3. Results and Discussion

3.1. Experimental Database

The experimental database is drawn from the database compiled by Sapkota et al. [39]. From this database, specimens were selected based on four scope criteria, namely non-prestressed members containing steel longitudinal reinforcement, steel fibers, and transverse reinforcement (stirrups), a shear span-to-depth ratio $a/d \geq 2.0$, an overall section height $h > 150$ mm, and a longitudinal reinforcement ratio in the range $2\% \leq \rho_l \leq 15\%$. The candidate beams were traced to their source studies, and two T-section beams without an identifiable source study were excluded. The scope criteria were then applied, and one beam with glass fiber-reinforced polymer longitudinal bars [65] and two beams with a published shear span-to-depth ratio below 2.0 [66] were excluded. The fiber volume fraction of one beam [67] and the compressive and yield strengths of six beams [68] were corrected to the values reported in the original publications. The final dataset comprises $N = 45$ beams from eight source studies. The selected specimens cover fiber volume fractions from 1.0% to 5.0% and compressive strengths from 114.5 to 185.2 MPa. The dataset includes 29 rectangular sections, 1 T-section, and 15 I-sections. The complete ranges of all key parameters are listed in Table 3.

Table 4 lists the eight source studies with the number of beams and the ranges of the main parameters of each study. Within a study, the specimens vary mainly in stirrup ratio, shear span-to-depth ratio, fiber volume fraction, and longitudinal reinforcement ratio. The rectangular sections come from six studies with web widths from 150 to 200 mm, and the I-sections come from two studies with web widths of 60 mm. As the fiber aspect ratio ranges from 20 to 87.5 across the studies, the fiber reinforcing index varies through both the fiber volume fraction and the fiber aspect ratio. Since the beams of one study share materials, geometry, and test procedures, all beams of one study are withheld together in the leave-one-study-out cross-validation of Section 2.6 to evaluate how the proposed model generalizes to new experimental campaigns.

Table 3. Range of parameters in the experimental database.

Category	Parameter	Minimum	Maximum
Geometry	h (mm)	250	500
	b_w (mm)	60	200
	a/d	2.0	4.0
Concrete	f'_c (MPa)	114.5	185.2
Longitudinal reinforcement	ρ_l (%)	3.6	12.8
Transverse reinforcement	ρ_{sv} (%)	0.13	2.09
	f_{sv} (MPa)	302	594
Fiber properties	ρ_f (%)	1.0	5.0
	l_f/d_f	20	87.5
Section type	Rectangular (29), T (1), I (15)		

Table 4. Source studies of the experimental database (parameter values as compiled by Sapkota et al. [39], with the corrections described in Section 3.1).

Source Study	Section	N	h (mm)	b_w (mm)	f'_c (MPa)	ρ_f (%)	l_f/d_f	a/d	ρ_{sv} (%)
Jin et al. [69]	Rectangular	2	250	150	116.7	2.0	59.1	2.26	0.45–0.74
Lim and Hong [30]	Rectangular	1	290	150	166.9	1.5	87.5	3.00	0.63
Liang et al. [70]	Rectangular	7	300	150	124.9–138.1	3.0, 5.0	38.9	2.21–2.35	0.19–0.75
Mészöly and Randl [71]	I	7	350	60	162.8–185.2	1.0, 2.0	75.0	3.20–3.50	0.87–2.09
Ji et al. [72]	I	8	500	60	128.4–154.5	1.5	59.1	2.00–4.00	0.24–0.47
Cao et al. [67]	Rectangular, T	9	250	150	127.1–160.6	2.0	59.1	2.25–3.00	0.13–0.50
Lu et al. [73]	Rectangular	5	250	150	114.5	2.5	20.0	2.18–2.54	0.17–0.74
Ma et al. [68]	Rectangular	6	350	200	119.4–132.1	1.0–3.0	65.0	2.00–2.50	0.17–0.50

The girders of Ji et al. [72], described as T-section girders in the source study, have a bottom flange in the database and are treated as I-sections.

3.2. Calibration and Identifiability

The model coefficients are obtained by minimizing the log-space least-squares objective $J = \sum_i [\ln \Theta_i]^2$, where $\Theta_i = V_{exp,i}/V_{pred,i}$ is the experimental-to-predicted shear capacity ratio for the i-th specimen. This objective penalizes overprediction and underprediction symmetrically and is consistent with the lognormal resistance model adopted in Section 3.8.

Since every specimen of the database contains fibers, the beam tests determine the fiber coefficient α_f only in combination with the baseline coefficient α_m, and any shear capacity attributed to the ψ_f-dependent fiber term can equally be absorbed by the ψ_f-independent baseline. When α_m, α_f, α_p, and the flange participation factor k are calibrated freely, the bootstrap median of α_f over 2000 resamples is 0.071, with a 95% confidence interval of [0.000, 0.170] that includes zero. Across the same resamples, the calibrated values of α_f and α_m have a correlation coefficient of −0.89. Furthermore, the database contains no companion pairs of beams differing only in fiber content or aspect ratio, and such pairs would be required to determine the ψ_f scaling from beam tests. Consequently, the beam tests constrain the total tensile stress $f_1 = f_{1,m} + f_{1,f}$, and the split between the two terms requires information independent of the beam database.

Therefore, the fiber coefficients are fixed from independent mechanics instead of regression. From the composite pullout expression $f_{1,f} = \eta\, \tau_b\, \rho_f\, (l_f/d_f)$ with $\eta = \eta_o \eta_l \eta_s$, the fiber coefficient is $\alpha_f = \eta\, \tau_b/\sqrt{f'_c}$. The efficiency factors adopted here ($\eta_o \in [0.405, 0.5]$, $\eta_l = 0.5$, $\eta_s \in [0.8, 1.0]$) and an interfacial bond stress τ_b of 9 to 12 MPa for straight steel

fibers in UHPC lead to an interval of $\alpha_f \in [0.107, 0.280]$ over the compressive strengths of the database. The bond stress range brackets the equivalent bond strength of about 10 MPa reported by Wille and Naaman [26]. The adopted value $\alpha_f = 0.19$ lies at the mid-range of this straight fiber interval. Since deformed fibers (hooked or twisted) develop bond strengths up to 47 MPa [26], this value constitutes a lower bound relative to deformed fibers, and the fiber term is expected to be conservative for specimens containing such fibers. The degradation parameter $\alpha_p = 135$ is obtained by mapping ε_x to the implied crack width and matching a 50% reduction in bridging stress at $w \approx 1.9$ mm. Lee et al. [58] expressed the reduction of the pullout stress of straight fibers with the crack width through the factor $(1 - 2w/l_f)^2$, and the factor halves at $w = 0.146\, l_f$, or 1.9 mm for the fiber length of 13 mm used in 25 of the 45 beams. In the MCFT [44], the average crack width is the product of the principal tensile strain and the average spacing of the diagonal cracks (s_θ), and the principal tensile strain is related to ε_x by the compatibility relation of Section 2.2. Hence, the implied crack width is given by:

$$w = s_\theta\, \varepsilon_1 = s_\theta\, \varepsilon_x \left(1 + \cot^2 \theta\right) \tag{18}$$

where s_θ is the average spacing of the diagonal cracks, taken as 150 mm. Minelli and Vecchio [74] adopted the measured average crack spacing of 150 mm in compression field analyses of high-performance concrete I-beams with stirrups, with and without steel fibers. The value of 150 mm lies below the typical upper limit of 300 mm given by Bentz et al. [45] for the spacing of diagonal cracks in members with longitudinal and transverse reinforcement. The 50% reduction of the fiber bridging stress occurs at $\alpha_p \varepsilon_x = 1$. For strains above 3.0×10^{-3}, θ reaches the upper bound of 50° and $1 + \cot^2 \theta = 1.70$. Therefore, Equation (18) results in $w = 1.70\, s_\theta / \alpha_p$ at the 50% reduction, and the value $\alpha_p = 135$ corresponds to $w = 1.89$ mm. For the mean converged state of the database ($\varepsilon_x = 8.43 \times 10^{-4}$ and $\theta = 34.9°$), Equation (18) results in $\varepsilon_1 = 2.57 \times 10^{-3}$ and $w = 0.39$ mm, with a fiber stress reduction of 10%, compared with a reduction of 56% for the baseline term. The largest converged strain of the database, 1.12×10^{-3}, corresponds to $w = 0.47$ mm and a fiber stress reduction of 13%. Accordingly, the fiber bridging stress degrades slowly over the crack widths of the database, whereas the baseline stress loses more than half of the initial value. After the fiber coefficients are fixed in this manner, only two parameters remain to be calibrated, namely the composite baseline coefficient $\alpha_m = 1.085$ (95% confidence interval [0.988, 1.181]) and the flange participation factor $k = 0.307$ (95% confidence interval [0.184, 0.470]).

The compatibility of the adopted fiber coefficient with the measured capacities is examined with the beam tests. Table 5 presents the calibration results for the lower bound, the adopted value, and the upper bound of this interval of α_f, with α_m and k recalibrated for each value. As α_f increases from 0.107 to 0.280, the calibrated α_m decreases from 1.241 to 0.925, and the mean fiber share of the sectional capacity increases from 11.5% to 29.5%. Over the same interval, the in-sample CoV varies only from 8.6% to 9.8%, and the LOOCV CoV varies from 9.0% to 10.2%. Therefore, the beam tests are compatible with the values tested over this interval, and the value of α_f is determined by the pullout mechanics. Under leave-one-study-out cross-validation, the CoV ranges from 12.5% to 12.9%, with the lowest value at the adopted $\alpha_f = 0.19$. In addition, the converged composite stresses f_1, from 5.95 to 9.55 MPa, are of the same magnitude as independent estimates of the localization tensile stress (Section 3.4). Accordingly, the total tensile stress implied by the fixed coefficients is consistent with the tensile capacity of UHPC.

Table 5. Calibration for the fiber bridging coefficient α_f over the interval from pullout mechanics, with α_m and k recalibrated for each value of α_f.

α_f	α_m	k	Mean V_f/V_{sect} (%)	CoV, In-Sample (%)	CoV, LOOCV (%)	CoV, Leave-One-Study-Out (%)
0.107 (lower bound)	1.241	0.304	11.5	8.6	9.0	12.9
0.190 (adopted)	1.085	0.307	20.3	8.9	9.3	12.5
0.280 (upper bound)	0.925	0.301	29.5	9.8	10.2	12.8

3.3. Moment Convention and Arch Action

Arch action supplements the sectional capacity in beams with a/d below approximately 2.5, and this effect is accounted for through the arch action factor of Zsutty [63], $e = \max(1, 2.5\,d/a)$. The factor is applied to the concrete and fiber contributions of the converged sectional solution, $V_{pred} = e\,(V_c + V_f) + V_s$, without introducing any fitted parameter. A controlled comparison confirms that the critical section moment of Equation (15) and the arch action factor serve distinct purposes and are not interchangeable. The critical section moment without the arch action factor does not remove the systematic a/d trend in the residuals since the term $2V$ in the numerator remains independent of a/d, whereas the arch action factor introduces the necessary a/d dependence. However, when both the moment at the middle of the shear span ($M = 0.5\,V\,a$, dependent on a/d) and the arch action factor are applied, the prediction is overcorrected and the direction of the bias is reversed. Therefore, the correct approach is to evaluate the longitudinal strain at the AASHTO critical section (where ε_x is independent of a/d) and to apply the arch action factor exactly once to the converged sectional solution. In addition, the variant of Kwak et al. [75], with an arch action threshold of 3.4 instead of 2.5, increases the CoV by 2.9 percentage points to 11.8% and lowers the calibrated resistance factor to $\phi^* = 0.735$.

3.4. Prediction Performance

Table 6 presents the in-sample and LOOCV performance of the proposed model, with every free coefficient refitted in each fold. In addition, the detailed accuracy metrics of the proposed model are presented in Table 7.

Table 6. Performance of the proposed model on $N = 45$ beams.

	Mean Θ	CoV (%)	R^2	MAPE (%)
Proposed, in-sample	1.007	8.9	0.840	7.5
Proposed, LOOCV	1.007	9.3	0.827	7.8

Table 7. Detailed prediction performance of the proposed EMCFT model ($N = 45$).

Metric	Value
Mean V_{exp}/V_{pred}	1.007
Standard deviation	0.090
Coefficient of variation (%)	8.9
Median V_{exp}/V_{pred}	0.996
Coefficient of determination (R^2)	0.840
Root mean square error (kN)	46.6
Mean absolute error (kN)	38.0
Mean absolute percentage error (%)	7.5
Predictions with $0.85 \le \Theta \le 1.15$ (%)	91.1
Predictions with $0.70 \le \Theta \le 1.30$ (%)	100.0
Conservative predictions, $V_{exp}/V_{pred} > 1.0$ (%)	48.9
Unconservative predictions, $V_{exp}/V_{pred} < 0.85$ (%)	4.4

Since the in-sample and LOOCV statistics differ by less than 0.5 percentage points in the CoV, the calibrated coefficients are insensitive to the removal of any single beam. When complete source studies were withheld, the mean ratio was 0.982 and the CoV was 12.5%, compared with a CoV of 17.6% for the PCI-UHPC provision [52] on the same beams (Section 3.7). Figure 3 shows the predicted versus experimental shear capacities, and Figure 4 shows the distribution of Θ and the DPC of the predictions. As can be seen in Figure 3, the predictions are distributed closely around the line of equality, with Θ from 0.85 to 1.15 for 91.1% of the beams. Convergence was achieved for all 45 beams in an average of 6.62 iterations. The mean crack angle at convergence was 34.9° and the mean longitudinal strain was 8.43×10^{-4}. The strut crushing limit did not govern for any specimen, and the total composite tensile stress $f_1 = f_{1,m} + f_{1,f}$ remained below the adopted 12 MPa limit in all cases, with a maximum of 9.55 MPa. For comparison, Tarawneh et al. [76] developed an empirical model of the localization tensile stress from 76 direct tension tests, $f_{t,\mathrm{loc}} \approx 0.279 + 0.035 f_c' + 3.40\,\rho_f\, l_f/d_f$ (with $\rho_f\, l_f/d_f$ as a fraction). For the 45 specimens, this model predicts values from 5.99 to 11.86 MPa. The converged composite stresses, 5.95 to 9.55 MPa, are of the same magnitude as these estimates, and the 12 MPa limit exceeds all of the estimates.

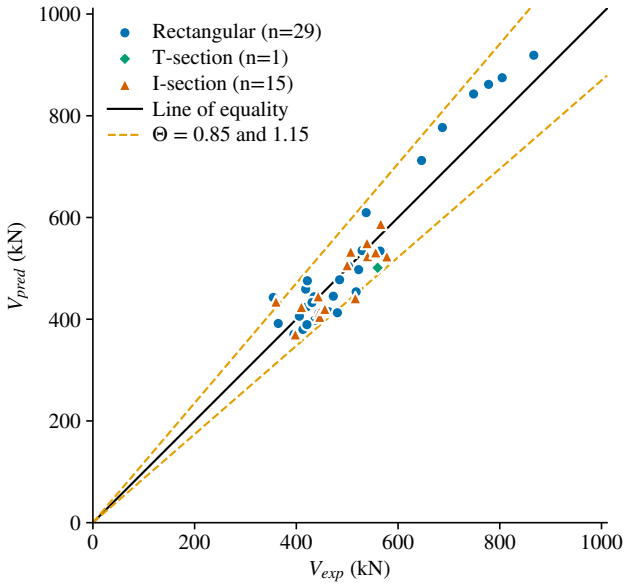


Figure 3. Predicted versus experimental shear capacity for the $N = 45$ beams (dashed lines indicate $V_{exp}/V_{pred} = 0.85$ and 1.15).

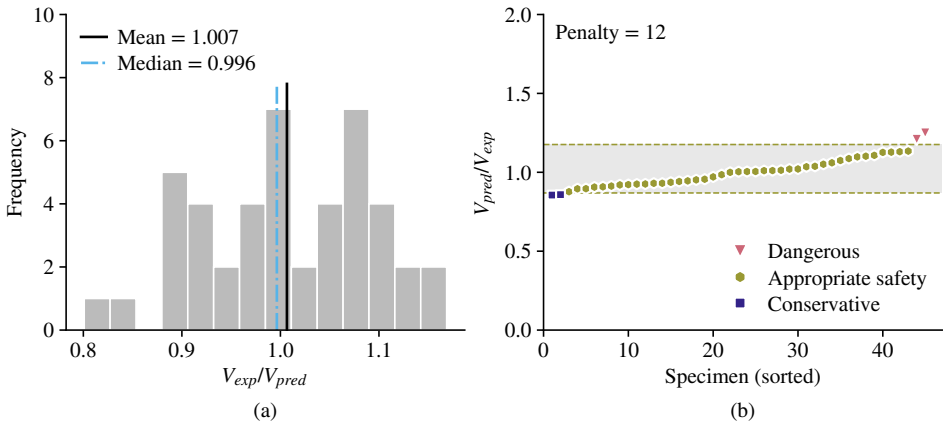


Figure 4. Prediction ratio of the proposed model, showing (**a**) the distribution of $\Theta = V_{exp}/V_{pred}$ and (**b**) the Demerit Points Classification, with the shaded band indicating the appropriate safety range.

Figure 5 shows the four beams with Θ outside the range from 0.85 to 1.15 as open circles, and Table 8 lists the source study and the properties of the four beams. Two beams are underpredicted (Θ > 1.15), namely a beam of Liang et al. [70] with a fiber volume fraction of 5%, above the 2% limit on the fiber volume fraction (Section 3.6.2), and an I-section beam of Mészöly and Randl [71] with a stirrup ratio of 1.31%. The two overpredicted beams (Θ < 0.85) are the beam with the lowest stirrup ratio of the database (0.13%, with a stirrup spacing of 1.48 d_v) and the most slender beam (a/d = 4.0). Accordingly, three of the four beams lie at the boundaries of the database in terms of the fiber volume fraction, the stirrup ratio, and the shear span-to-depth ratio. The four beams come from four different source studies, and the Spearman correlation between Θ and the ratio of the stirrup spacing to the effective shear depth is not significant (ρ = 0.005, p = 0.98).

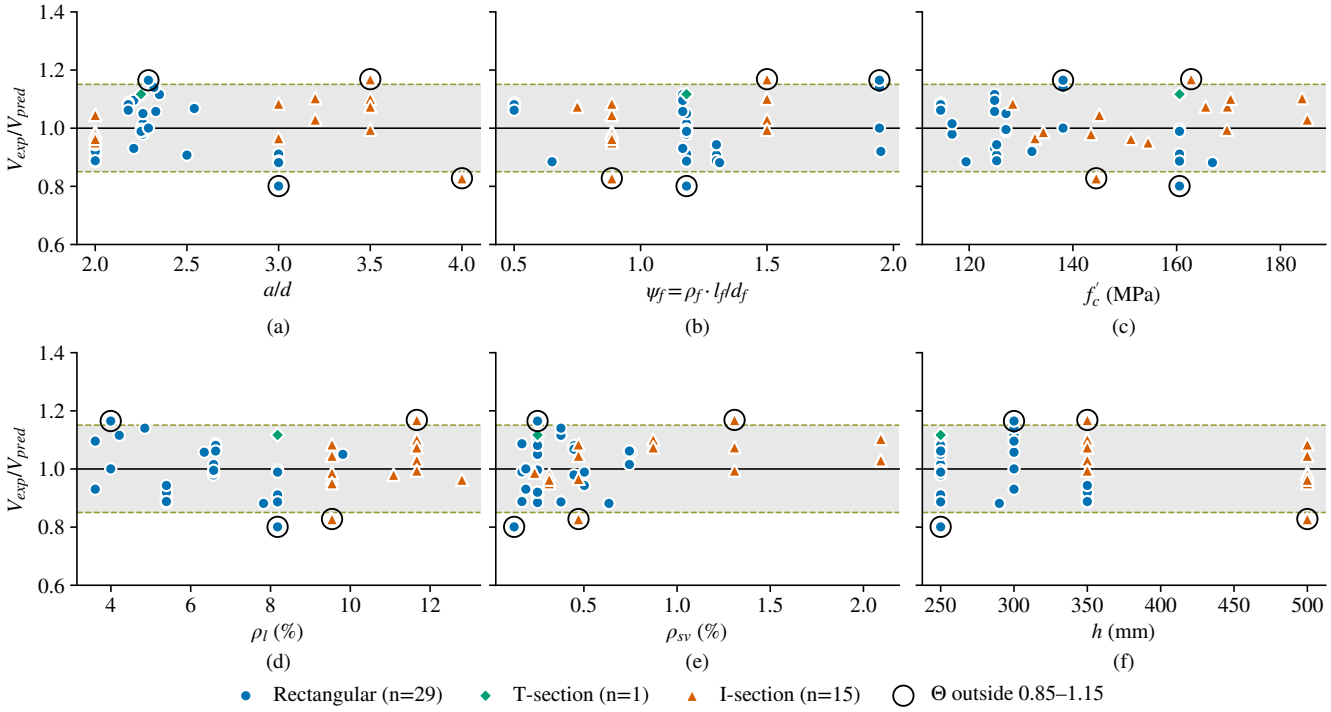


Figure 5. V_{exp}/V_{pred} ratio versus (**a**) the shear span-to-depth ratio (a/d), (**b**) the fiber reinforcing index (ψ_f), (**c**) the compressive strength (f_c'), (**d**) the longitudinal reinforcement ratio (ρ_l), (**e**) the stirrup ratio (ρ_{sv}), and (**f**) the section height (h), with open circles marking the Θ values outside the range from 0.85 to 1.15 and the shaded band indicating the appropriate safety range.

Table 8. Beams with Θ = V_{exp}/V_{pred} outside the range from 0.85 to 1.15 (s/d_v is the ratio of the stirrup spacing to the effective shear depth).

Source Study	Section	h (mm)	a/d	ρ_f (%)	l_f/d_f	ρ_l (%)	ρ_{sv} (%)	s/d_v	Θ
Cao et al. [67]	Rectangular	250	3.00	2.0	59.1	8.18	0.13	1.48	0.801
Ji et al. [72]	I	500	4.00	1.5	59.1	9.54	0.47	0.25	0.828
Liang et al. [70]	Rectangular	300	2.29	5.0	38.9	3.99	0.25	0.62	1.165
Mészöly and Randl [71]	I	350	3.50	2.0	75.0	11.67	1.31	0.71	1.169

The variation of the prediction ratio Θ with a/d is shown in Figure 5a. The binned means are 1.014, 0.964, and 1.040 for the three a/d subgroups, all within [0.95, 1.10]. To characterize this residual rigorously, four statistical tests were conducted. The magnitude-based tests find no significant slope. The ordinary least-squares slope is +0.0037 with a 95% confidence interval of [−0.0463, +0.0538] (p = 0.88), and a permutation test on the slope

with 10,000 permutations confirms this result ($p = 0.886$). Similarly, the rank-based tests are not significant at the 5% level, with Spearman $\rho = +0.207$ ($p = 0.172$) and Kendall's $\tau_b = +0.168$ ($p = 0.119$). Within the band $2.0 \leq a/d < 2.5$, containing 29 of the 45 beams, the 10 beams at $a/d = 2.0$ with the largest arch action factor ($e = 1.25$) have a mean Θ of 0.947, whereas the remaining 19 beams in the band have a mean Θ of 1.050, and Section 3.6.1 discusses the difference. No residual bias is observed with respect to section type or the fiber reinforcing index ψ_f (Table 9 and Figure 5b). The ratio Θ increases with the fiber volume fraction ρ_f (Spearman $\rho = +0.374$, $p = 0.011$), consistent with the conservative 2% limit on ρ_f, whereas the trend with the fiber aspect ratio l_f/d_f is not significant ($\rho = -0.284$, $p = 0.059$) (Section 3.6.2). Subgroup performance statistics and corresponding resistance factors are presented in Table 9.

Table 9. Subgroup performance and subgroup resistance factors (the column $\Theta < 0.85$ gives the fraction of unconservative predictions, and R_k/V_{pred} is the characteristic (5th-percentile) resistance ratio, $\lambda_R(1 - 1.645\,V_R)$).

Subgroup	N	Mean Θ	CoV (%)	$\Theta < 0.85$ (%)	ϕ^*	R_k/V_{pred}
Overall	45	1.007	8.9	4.4	0.776	0.825
Rectangular	29	0.994	9.3	3.4	0.761	0.810
T-section †	1	1.117	N/A	0.0	N/A	N/A
I-section	15	1.024	8.2	6.7	0.801	0.849
$\rho_f \leq 1.5\%$	12	0.977	8.5	8.3	0.759	0.805
$\rho_f > 1.5\%$	33	1.017	8.9	3.0	0.784	0.833
$\psi_f < 1.0$	16	1.014	7.8	6.2	0.797	0.845
$\psi_f \geq 1.0$	29	1.003	9.6	3.4	0.762	0.812
$2.0 \leq a/d < 2.5$	29	1.014	7.6	0.0	0.802	0.849
$2.5 \leq a/d < 3.5$	10	0.964	10.6	10.0	0.717	0.767
$a/d \geq 3.5$	6	1.040	11.4	16.7	0.761	0.817

† Insufficient sample ($N < 5$), excluded from the basis of the design recommendation.

3.5. Shear Contribution Decomposition

The three-component formulation enables a transparent decomposition of the predicted shear capacity into its constituent mechanisms, as shown in Figure 6. On average, the composite baseline contributes 59.6% of the converged sectional capacity, the separable fiber term contributes 20.3%, and the stirrups contribute the remaining 20.1%. The fiber share is strongly dependent on the fiber reinforcing index ψ_f, spanning from 10.8% to 23.2% across the ψ_f bins, with the lowest values occurring at $\psi_f \approx 0.6$ and the contribution plateauing above $\psi_f \approx 1.0$. Therefore, the full range is reported in addition to the average share. The percentages are calculated from the model equations with the fiber coefficients fixed from pullout mechanics, since the beam tests provide only the total capacity (Section 3.2). Since $f_{1,m}$ is a composite (fibrous UHPC) tension stiffening baseline, the decomposition distinguishes a dosage-independent composite baseline from a dosage-sensitive fiber increment, instead of partitioning the capacity between fiber-free concrete and fibers.

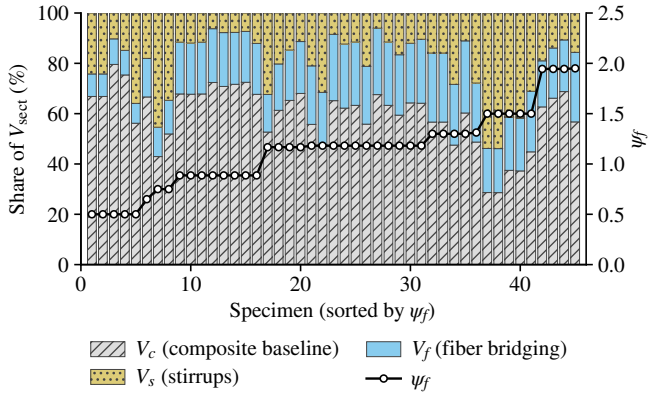


Figure 6. Model-based decomposition of the converged sectional shear capacity V_{sect} (before the arch action factor) into composite baseline (V_c), fiber (V_f), and stirrup (V_s) shares for the specimens sorted by the fiber reinforcing index ψ_f (line, right axis).

3.6. Sensitivity to Key Input Parameters

The variation of the V_{exp}/V_{pred} ratio with the principal design parameters is examined to identify systematic biases. Table 9 presents the subgroup statistics, including the fraction of unconservative predictions ($\Theta < 0.85$), and Figure 5 shows the variation of Θ with each design parameter. Since the model is calibrated to be essentially unbiased (mean $\Theta = 1.007$) instead of conservatively biased, a fraction of predictions necessarily falls below 0.85, and the margin of safety against this scatter is provided by the resistance factor calibrated in Section 3.8, not by a built-in bias.

3.6.1. Effect of the Shear Span-to-Depth Ratio

The shear span-to-depth ratio governs the relative importance of beam action and arch action. For beams with $2.0 \leq a/d < 2.5$ (29 beams), the model achieves a mean ratio of 1.014 with a CoV of 7.6% and no unconservative prediction ($\Theta < 0.85$) (Figure 5a), and this subgroup, constituting about two thirds of the database, benefits directly from the arch action factor of Equation (17). For $2.5 \leq a/d < 3.5$ (10 beams), the mean ratio is 0.964 with a CoV of 10.6%, and the corresponding subgroup resistance factor ($\phi^* = 0.717$) exceeds the design recommendation. For $a/d \geq 3.5$ (6 beams), the mean ratio is 1.040 with a CoV of 11.4%. The statistical tests of the a/d trend are presented in Section 3.4. The 10 beams at $a/d = 2.0$ come from two source studies with the same arch action factor ($e = 1.25$). The five I-section beams of Ji et al. [72] have a mean Θ of 0.986, whereas the five rectangular beams of Ma et al. [68] have a mean Θ of 0.908. Since both studies have the same arch action factor, the difference between the studies indicates that the lower mean ratio at $a/d = 2.0$ is not caused by the arch action factor alone. The 10 beams have a CoV of 5.3% and a subgroup resistance factor of $\phi^* = 0.775$, above the recommended value of 0.70. Therefore, the predictions at $a/d = 2.0$ remain within the reliability calibration of Section 3.8.

3.6.2. Effect of Fiber Content

For beams with $\rho_f > 1.5\%$ (33 beams), the model achieves a mean ratio of 1.017 with a CoV of 8.9%, and for $\rho_f \leq 1.5\%$ (12 beams) a mean ratio of 0.977 with a CoV of 8.5%; the difference between the two groups is not significant (Welch $p = 0.174$), and neither group exhibits elevated scatter. However, when ρ_f is considered as a continuous variable, Θ increases with ρ_f (Spearman $\rho = +0.374$, $p = 0.011$), and the 13 beams with $\rho_f > 2\%$ have a mean Θ of 1.062, indicating that the limit $\rho_{f,\text{eff}} = \min(\rho_f, 0.02)$ is conservative for these beams. The trend with the aspect ratio l_f/d_f is not significant (Spearman $\rho = -0.284$, $p = 0.059$), and the difference between the groups with ψ_f below and above 1.0 is not

significant (Welch $p = 0.685$; Figure 5b). For the low-dosage subgroup, the resistance factor of 0.759 remains above the recommended $\phi = 0.70$. The beam of Liang et al. [70] with a fiber volume fraction of 5% is one of the two underpredicted beams of Table 8, consistent with the conservative 2% limit on ρ_f.

3.6.3. Effect of Section Geometry

The database includes 29 rectangular sections, 1 T-section, and 15 I-sections. The rectangular and I-section subgroups perform similarly (mean ratios of 0.994 and 1.024, CoVs of 9.3% and 8.2%), and the difference between the two subgroups is not significant (Welch $p = 0.289$). The similar performance of the two subgroups results from the calibrated effective width correction of Equation (11), and the correction restores the flange participation that a web-only formulation omits. When all shear terms are computed on b_w alone, the I-sections are systematically underpredicted (mean Θ of 1.114, compared with 0.950 for the rectangular sections, with α_m recalibrated). Since the database contains a single T-section beam [67], predicted with $\Theta = 1.117$, the design recommendation covers rectangular sections and I-sections.

3.6.4. Effect of Concrete Strength and Reinforcement Parameters

The variation of Θ with compressive strength (Figure 5c) reveals no systematic trend over the range from 114.5 to 185.2 MPa (Spearman $p = 0.931$), confirming that the $\sqrt{f'_c}$ normalization adopted in both $f_{1,m}$ and $f_{1,f}$ adequately accounts for the effect of concrete strength. Similarly, Figure 5d,e show no discernible trend with respect to ρ_l or ρ_{sv}. In addition, Θ shows no significant trend with the section height (Figure 5f; Spearman $\rho = -0.145$, $p = 0.343$), with a mean Θ of 1.021 for $h < 350$ mm and 0.991 for $h \geq 350$ mm. The absence of systematic biases with respect to f'_c, ρ_l, ρ_{sv}, and h indicates that the SMCFT expressions for ε_x and θ remain appropriate for UHPC and that the proposed constitutive equations do not introduce parameter-dependent distortions.

3.7. Comparison with Existing Models

The performance of the proposed EMCFT model is compared with four existing models, namely the PCI-UHPC provision applied as published, the FHWA [41] and AFGC [60,61] provisions with estimated tensile inputs, and the standard SMCFT, each evaluated on the identical set of $N = 45$ beams. Since the FHWA and AFGC provisions require a measured tensile input that is unavailable at the design stage, the two provisions are implemented here with the fiber tensile stress estimated from the fiber volume fraction, the fiber aspect ratio, and the compressive strength (ρ_f, l_f/d_f, f'_c). Therefore, the two implementations are referred to as the FHWA-based and AFGC-based models. Specifically, the FHWA-based implementation replaces the measured $f_{t,\mathrm{loc}}$ with the estimator $0.75\sqrt{f'_c}\,\rho_f(l_f/d_f)$ (retaining $\gamma_u = 0.85$), evaluates the crack angle from Equation (13) with the mid-depth strain of Equation (15) in place of the iterative strain compatibility solution of the provision, takes the stirrup stress at yield instead of from the computed transverse strain, and applies the strut limit of Equations (7) and (8). Similarly, Tarawneh et al. [76] estimated $f_{t,\mathrm{loc}}$ from f'_c and $\rho_f\, l_f/d_f$ to apply the FHWA provisions to 198 girders. The AFGC-based implementation replaces the fiber tensile stress σ_f with $0.60\sqrt{f'_c}\,\rho_f(l_f/d_f)$ at the fixed minimum angle $\theta = 30°$ permitted by the standard. All three terms of the provision are retained, with the partial safety factors set to unity for comparison [60,61]. For reinforced members without axial load ($k_a = 1$), the concrete term is $V_{Rd,c} = 0.21\,k_a\sqrt{f_{ck}}\,b_w\,d$, where f_{ck} is the characteristic compressive strength. Among the three UHPC provisions, the PCI-UHPC provision [52] is the only one that can be implemented exactly as published, since this provision specifies

a design constant (f_{rr} = 5.2 MPa for UHPC meeting the minimum PCI-UHPC tensile requirements) in place of a measured tensile input. The provision is implemented with its own longitudinal strain expression, crack angle relation $\theta = 29^\circ + 3500\,\varepsilon_s$ with the published strain bounds, and upper limit on the shear capacity. The SMCFT is implemented as published by Bentz et al. [45], with $V_c = \beta\sqrt{f'_c}\,b_w\,d_v$, $\beta = 0.4/(1 + 1500\,\varepsilon_x)$, and the $0.25f'_c\,b_w\,d_v$ limit, and without a fiber term.

Accordingly, the provisions are compared at the design stage, when no measured tensile property of the mix is available. Under this condition, the FHWA and AFGC provisions operate with estimated inputs instead of the measured direct tension or flexural properties required by the provisions. Consequently, the FHWA-based and AFGC-based results represent the performance of the provisions at the design stage and not the accuracy of the provisions with measured tensile inputs. Since the PCI-UHPC provision is applied with its intended inputs, this provision provides the most direct comparison between design stage models. The SMCFT without a fiber term is included only to illustrate the magnitude of the capacity derived from the fibers. The results of the comparative analysis are presented in Table 10 and shown in Figures 7 and 8.

As shown in Figure 7a, the predictions of the proposed EMCFT model are clustered tightly along the line of equality, with an R^2 of 0.840 computed on the full 45-beam dataset. The PCI-UHPC provision (Figure 7b) underestimates the shear capacity systematically, with nearly all predictions below the line of equality. The FHWA-based model (Figure 7c) exhibits substantially wider scatter, with several points that deviate markedly from the line of equality, consistent with its much lower R^2 of −0.327. The AFGC-based model (Figure 7d) shows both the widest scatter and a systematic shift above the line of equality (mean V_{exp}/V_{pred} = 0.883), producing many severe overpredictions. The standard SMCFT model (Figure 7e) shows all points far below the line of equality, reflecting the complete absence of any fiber contribution.

As can be seen in Figure 8 and Table 10, the proposed EMCFT model achieved the lowest total DPC penalty of 12, compared with 30 for the PCI-UHPC provision, 59 for the FHWA-based model, 149 for the AFGC-based model, and 85 for the SMCFT. No EMCFT prediction fell in the extremely dangerous or extremely conservative categories, and 91.1% (41 out of 45) were classified as appropriate safety, 4.4% (2 out of 45) as conservative, and 4.4% (2 out of 45) as dangerous (Figure 8a).

Table 10. Comparison of prediction performance and DPC analysis for five models.

Model	Mean Θ	SD	CoV (%)	R^2	DPC Classification					Penalty
					ED	D	AS	C	EC	
EMCFT (proposed)	1.007	0.090	8.9	0.840	0	2	41	2	0	12
PCI-UHPC (as published)	1.265	0.223	17.6	−0.017	0	0	15	30	0	30
FHWA (est. $f_{t,\mathrm{loc}}$)	1.173	0.366	31.2	−0.327	0	8	19	17	1	59
AFGC (est. σ_f)	0.883	0.293	33.2	−3.305	1	26	9	9	0	149
SMCFT (no fiber term)	2.704	0.700	25.9	−6.532	0	0	0	5	40	85

ED = extremely dangerous; D = dangerous; AS = appropriate safety; C = conservative; EC = extremely conservative; SD = standard deviation. PCI-UHPC uses f_{rr} = 5.2 MPa. FHWA and AFGC are implemented with the tensile input estimated from the fiber properties and the compressive strength, and the AFGC-based implementation includes all three terms of the provision and is evaluated at the fixed minimum angle $\theta = 30^\circ$ permitted by the standard. SMCFT is applied without a fiber term and is included only to illustrate the magnitude of the fiber-derived capacity.

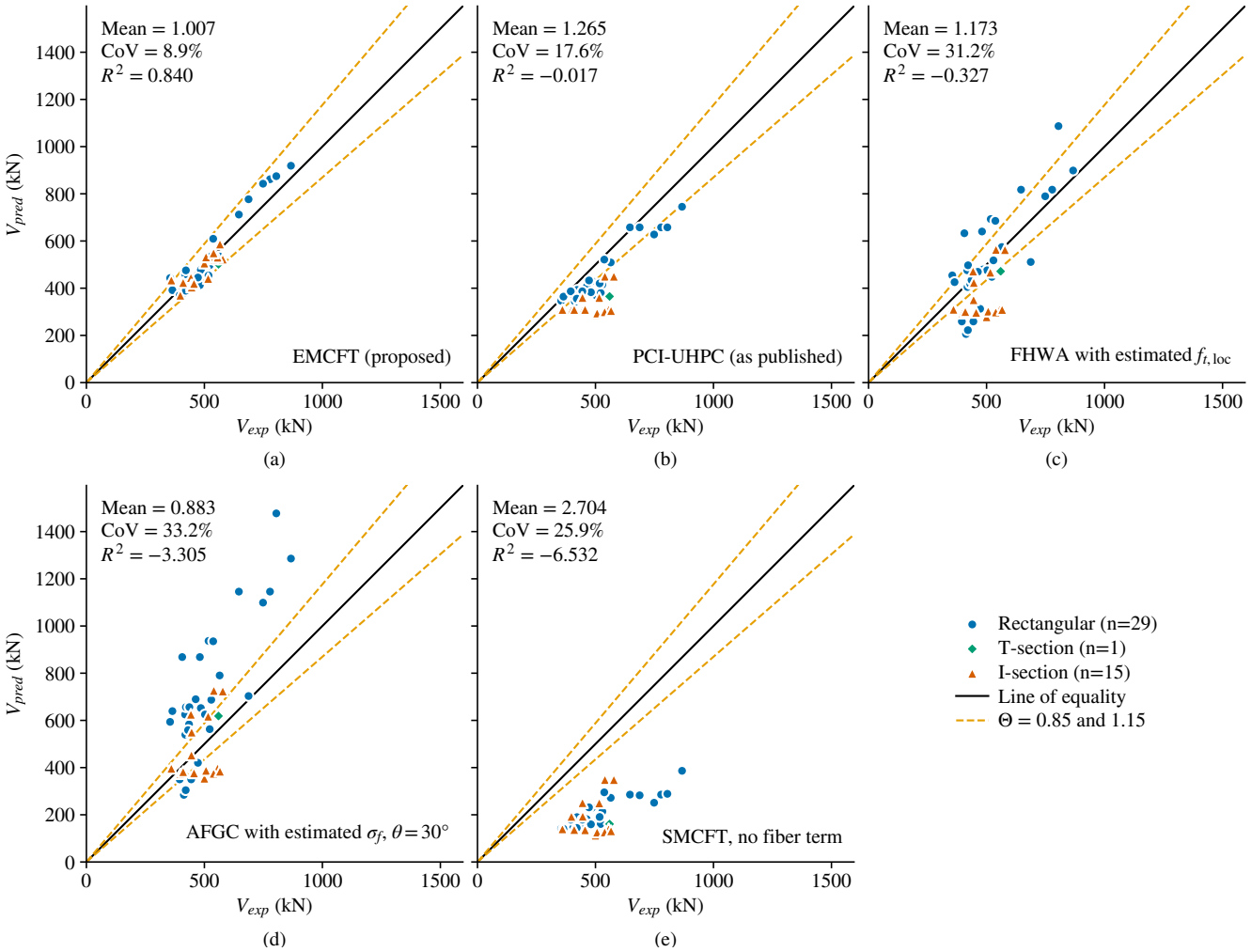


Figure 7. Predicted versus experimental shear capacity of the five models, showing (**a**) EMCFT (proposed), (**b**) PCI-UHPC as published, (**c**) FHWA with estimated $f_{t,\mathrm{loc}}$, (**d**) AFGC with estimated σ_f at $\theta = 30°$, and (**e**) SMCFT without a fiber term (dashed lines indicate $V_{exp}/V_{pred} = 0.85$ and 1.15, and the text in each panel gives the mean and CoV of V_{exp}/V_{pred} and the R^2 of the model).

The PCI-UHPC provision applied exactly as published has a mean ratio of 1.265, a CoV of 17.6%, an R^2 of −0.017, and a total penalty of 30 (Figure 8b). The residual tensile strength of the provision (f_{rr} = 5.2 MPa) is independent of the fiber content and aspect ratio, whereas the tensile term of the proposed model depends on the fiber parameters. For comparison, the proposed model attains a 60% lower penalty (12 versus 30), a 49% lower CoV (8.9% versus 17.6%), and a higher R^2 (0.840 versus −0.017).

The FHWA-based model resulted in a mean V_{exp}/V_{pred} ratio of 1.173 and a CoV of 31.2%. The higher CoV and the lower R^2 of −0.327 indicate greater scatter and a weaker correlation with the experimental data than those of the proposed model. From a safety perspective, 17.8% of predictions (8 out of 45) were classified as dangerous in the DPC analysis, for a total penalty of 59 (Figure 8c), and this large number of dangerous predictions is a direct consequence of the high scatter. The AFGC-based model produced the highest DPC penalty among the five models, with a mean ratio of 0.883 (unconservative on average), a CoV of 33.2%, and a negative R^2 of −3.305. The DPC analysis classifies one prediction as extremely dangerous and 26 as dangerous, for a total penalty of 149 (Figure 8d), more than twelve times that of the proposed model. This behavior can be attributed to three factors acting together. First, the fixed minimum crack angle of $\theta = 30°$ is shallower than the crack angle the strain state implies for most of these beams, inflating the cot θ projection.

Second, the constant fiber stress of the AFGC-based implementation does not degrade with the strain state, unlike the measured $\sigma(w)$ law of the published provision. Third, the additive concrete term $V_{Rd,c}$ compounds the first two effects. The result is a systematic overprediction with large scatter, heavily penalized by the DPC.

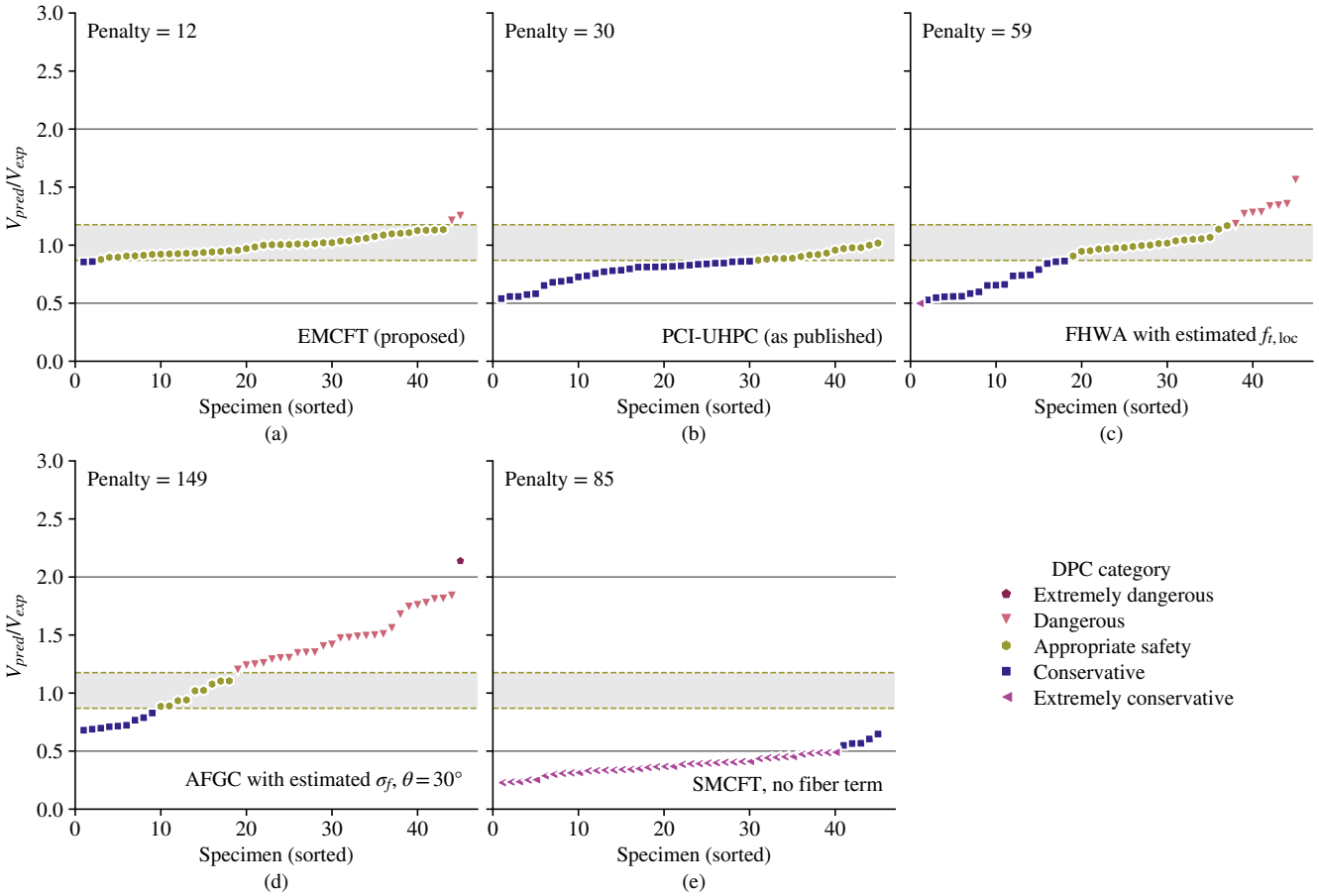


Figure 8. Demerit Points Classification of the five models, showing (**a**) EMCFT (proposed), (**b**) PCI-UHPC as published, (**c**) FHWA with estimated $f_{t,\mathrm{loc}}$, (**d**) AFGC with estimated σ_f at $\theta = 30°$, and (**e**) SMCFT without a fiber term (the shaded band indicates the appropriate safety range, and the solid lines at 0.5 and 2.0 mark the limits of the extremely conservative and extremely dangerous categories).

The standard SMCFT model, applied without any fiber contribution term, resulted in a mean ratio of 2.704, indicating that the experimental capacity was on average more than twice the predicted capacity. This large underprediction confirms that the fiber-derived post-cracking tensile capacity of UHPC, captured in the proposed model through the composite tension stiffening baseline and the explicit fiber term, provides a substantial fraction of the shear resistance and must be represented explicitly. All SMCFT predictions were either conservative (5) or extremely conservative (40), and no SMCFT prediction fell in the appropriate safety or dangerous categories, as shown in Figure 8e.

3.8. Resistance Factor Calibration

The model uncertainty, defined as $\Theta = V_{exp}/V_{pred}$, is well described by a lognormal distribution. The Kolmogorov–Smirnov test results in a p-value of 0.707, and the Anderson–Darling statistic of 0.468 is below the 5% critical value of 0.739. Figure 9a shows the fitted distribution, and Figure 9b shows the normal Q-Q plot of $\ln \Theta$. The resulting bias factor is $\lambda_R = 1.007$ with a model coefficient of variation $V_\theta = 8.9\%$. The combination of the

model uncertainty with the material variability (5%) [77] and the fabrication variability (4%) [77–79] leads to a total resistance CoV of $V_R = 11.0\%$.

The lognormal parameters underlying the distributional tests are estimated from the log-transformed ratios, as given by:

$$\varepsilon_i = \ln \Theta_i, \qquad \mu_\varepsilon = \frac{1}{N}\sum_{i=1}^{N} \varepsilon_i, \qquad \sigma_\varepsilon^2 = \frac{1}{N-1}\sum_{i=1}^{N} (\varepsilon_i - \mu_\varepsilon)^2 \tag{19}$$

The resulting values are $\mu_\varepsilon = 0.003$ and $\sigma_\varepsilon = 0.091$. The bias factor λ_R is taken as the sample mean of Θ and V_θ as its sample coefficient of variation, and the total resistance coefficient of variation combines the model uncertainty with the material variability ($V_m = 0.05$) and the fabrication variability ($V_{fab} = 0.04$), as given by:

$$V_R = \sqrt{V_\theta^2 + V_m^2 + V_{fab}^2} \tag{20}$$

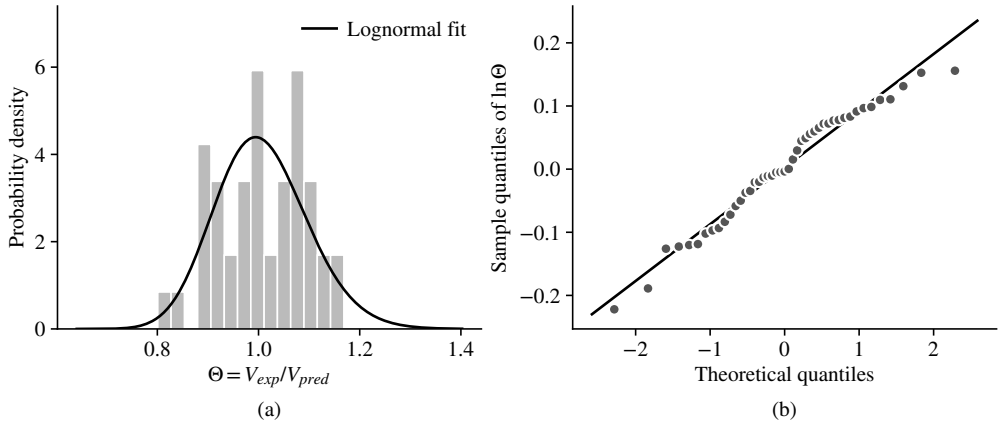


Figure 9. Model uncertainty distribution, showing (**a**) the histogram of $\Theta = V_{exp}/V_{pred}$ with the fitted lognormal probability density function and (**b**) the normal Q-Q plot of $\ln \Theta$.

Nowak and Szerszen [77] adopted coefficients of variation of 0.04 for the width and depth of beams, 0.05 for the yield strength of reinforcing steel, and 0.10 for the compressive strength of concrete in the calibration of ACI 318. Since the concrete and fiber contributions are proportional to $\sqrt{f'_c}$, a coefficient of variation of 0.10 for f'_c corresponds to approximately 0.05 for the two contributions, equal to the value for the stirrups. For a unit nominal total load with a dead-to-total load ratio $\alpha = D_n/(D_n + L_n)$, the factored load of the $1.2D + 1.6L$ combination of ACI 318-19 [53] is $U(\alpha) = 1.2\,\alpha + 1.6\,(1 - \alpha)$. The load statistics of Szerszen and Nowak [80] are adopted. The dead load has a bias factor of $\lambda_D = 1.05$ with a CoV of 0.10, and the 50-year maximum live load has a bias factor of $\lambda_L = 1.00$ with a CoV of 0.18. When the resistance and the load are expressed in the lognormal format, the reliability index for a trial resistance factor ϕ is given by:

$$\beta(\phi, \alpha) = \frac{\ln\left[\lambda_R\, U(\alpha) \,/\, \left(\phi\, \bar{Q}(\alpha)\right)\right]}{\sqrt{\ln\left[(1 + V_R^2)(1 + V_Q^2(\alpha))\right]}} \tag{21}$$

where $\bar{Q}(\alpha) = \lambda_D\,\alpha + \lambda_L\,(1 - \alpha)$ is the mean total load and $V_Q(\alpha)$ is the CoV of the total load. The optimal resistance factor ϕ^* is determined through minimization of the least-squares method (LSM) criterion, as given by:

$$\mathrm{LSM}(\phi) = \frac{1}{n_\alpha}\sum_{i=1}^{n_\alpha} \left[\beta(\phi, \alpha_i) - \beta_T\right]^2 \tag{22}$$

over $\alpha \in \{0.0, 0.1, \ldots, 1.0\}$, where $\beta_T = 3.5$ is the target reliability index for shear-critical members [80]. The conservative alternative, $\phi_{min} = \min_\alpha \phi(\alpha) = 0.685$, occurs at $\alpha = 1.0$ (pure dead load) for this load combination.

A first-order second-moment calibration is performed at a target reliability index $\beta_T = 3.5$ using the ACI 318 load factors and statistical bias values. The resulting least-squares resistance factor is $\phi^* = 0.776$ with a 95% confidence interval of [0.741, 0.814] obtained from 10,000 bootstrap resamples. Figure 10a shows the reliability index against the resistance factor ϕ for dead-to-total load ratios ranging from $\alpha = 0.0$ to 1.0, Figure 10b shows the least-squares criterion with its minimum at $\phi^* = 0.776$, and Figure 10c shows the subgroup resistance factors. For typical building load combinations with a dead-to-total load ratio $\alpha \leq 0.6$, a resistance factor of $\phi = 0.70$ is supported by the calibration. For bridge girders, with dead-to-total load ratios of about 0.5 for spans of 5 to 25 m and about 0.7 for spans of 25 to 80 m [81], the same value of $\phi = 0.70$ remains supported under the ACI 318 load model, since the calibrated resistance factor is at least 0.742 for ratios from 0.60 to 0.85. The calibrated value of 0.776 is close to the ACI 318 strength reduction factor for shear of 0.75. The recommendation rests on the global calibration, and the subgroup resistance factors in Table 9 are consistency checks computed on small subsets. The single T-section beam has no separate subgroup resistance factor.

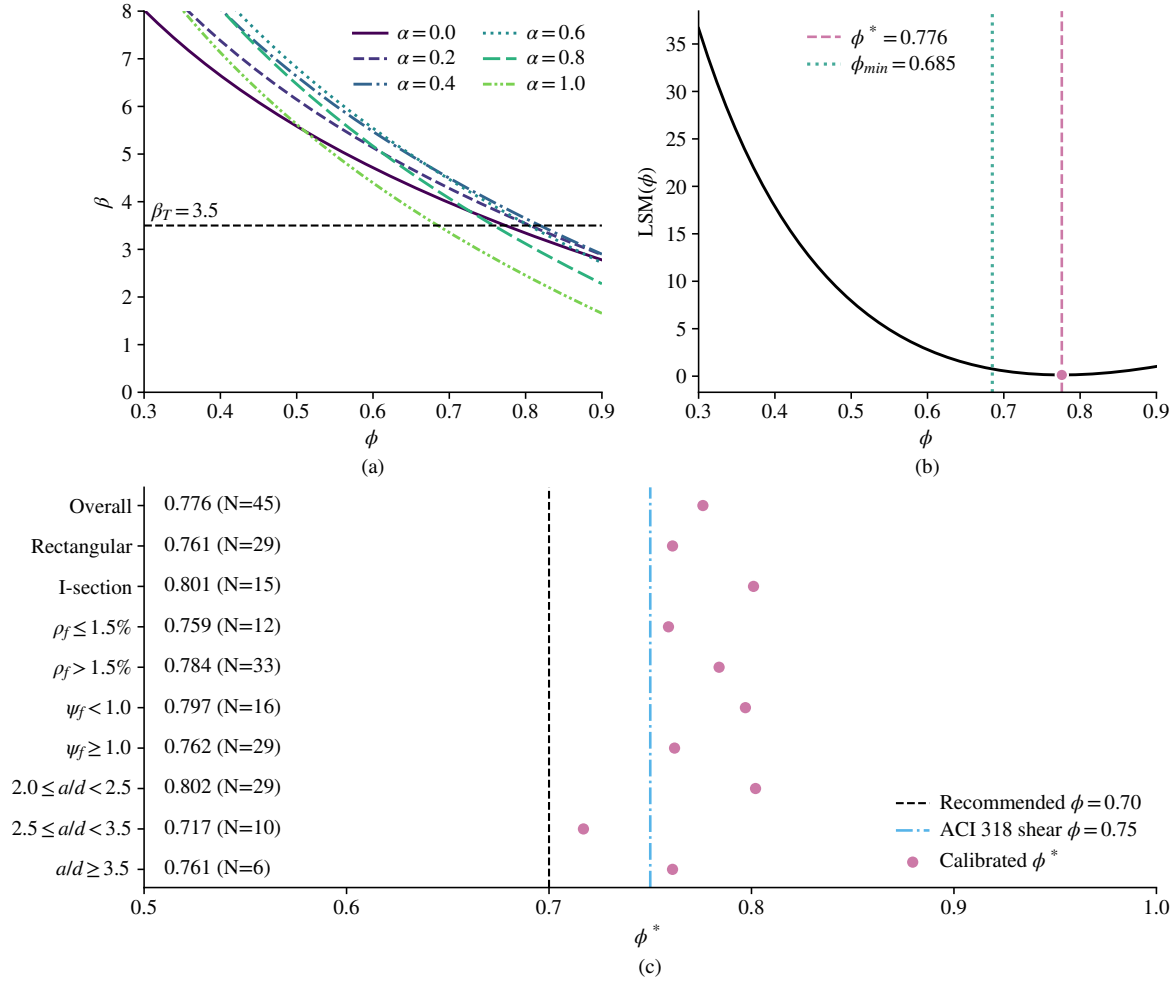


Figure 10. Reliability calibration results, showing (**a**) the reliability index β versus the resistance factor ϕ for dead-to-total load ratios α from 0.0 to 1.0 with the target $\beta_T = 3.5$ as a horizontal dashed line, (**b**) the least-squares calibration criterion of Equation (22) with its minimum at $\phi^* = 0.776$ and the conservative minimum $\phi_{min} = 0.685$, and (**c**) the calibrated resistance factors ϕ^* of the subgroups with the recommended $\phi = 0.70$ and the ACI 318 strength reduction factor for shear of 0.75.

The resistance factor of $\phi = 0.70$ is recommended for preliminary design and parametric studies within the scope of the database. The bootstrap 95% confidence interval of ϕ^*, from 0.741 to 0.814, quantifies the sampling uncertainty of the calibration. Subgroups with fewer than five specimens are excluded from the basis of the recommendation, and the recommendation applies to rectangular sections and I-sections within the ranges of Table 3. Every subgroup with at least five specimens has a resistance factor from 0.717 to 0.802 (Table 9), consistent with the recommendation. Within this scope, the value of 0.70 provides a resistance factor for the design stage, before the measured tensile properties required by the FHWA and AFGC provisions are available. The adoption of the resistance factor in a design provision would follow a calibration on a larger database with the load model of the target design code.

The calibration uses the load factors and load statistics of building design, and the application to bridges requires a calibration with a bridge load model. In the AASHTO LRFD Bridge Design Specifications [82], the Strength I load combination applies load factors of 1.25 to the dead load of structural components and 1.75 to the vehicular live load with the dynamic load allowance, compared with 1.2 and 1.6 in ACI 318-19 [53]. The AASHTO live load model is based on statistics for a design life of 75 years, whereas the building calibration uses the 50-year maximum live load. In addition, the statistics of the vehicular live load with the dynamic load allowance differ from the building live load statistics of Szerszen and Nowak [80]. A calibration with the AASHTO load factors and the vehicular live load statistics would provide a resistance factor specific to bridge design. Many experimental programs on UHPC bridge girders involve prestressed members [34,37], and Section 3.9 discusses the application of the proposed model to prestressed members.

3.9. Application to Prestressed Members

The proposed model was calibrated and validated on non-prestressed beams, whereas a large part of the experimental research on UHPC shear involves prestressed members [34,35,37]. The general form of the longitudinal strain in Equation (14) contains the prestressing terms $A_{ps}f_{po}$ in the numerator and E_pA_{ps} in the denominator. Therefore, the formulation accommodates prestressing without a change in structure. For a prestressed member, the term $A_{ps}f_{po}$ reduces ε_x, and a lower ε_x produces a flatter crack angle through Equation (13) and a larger $\cot\theta$ in Equations (4)–(6). In addition, a lower strain reduces the degradation of $f_{1,m}$ and $f_{1,f}$ in Equations (9) and (10). As a result, the predicted shear capacity increases with the effective prestress. For highly prestressed members, the numerator of Equation (14) can become negative, and the augmented denominator of Equation (16) with the axial stiffness of the concrete would govern, a condition that does not occur for the non-prestressed beams of the database. For draped tendons, the vertical component of the prestressing force (V_p) would add to the resistance, consistent with the AASHTO LRFD sectional model [82].

4. Conclusions

This study proposes an Enhanced Modified Compression Field Theory (EMCFT) that predicts the shear capacity of ultra-high-performance concrete (UHPC) beams with steel fibers and stirrups from inputs known at the design stage, with the fiber volume fraction, the fiber aspect ratio, and the compressive strength in place of a measured tensile property. The principal tensile stress is decomposed into a composite tension stiffening baseline and a separable fiber bridging term, with the fiber coefficients fixed from independent pullout mechanics. The longitudinal strain is evaluated at the AASHTO critical section, and arch action is accounted for through an arch action factor applied to the concrete and fiber contributions. Consequently, the prediction ratio shows no significant trend with the shear span-to-depth ratio. For 45 beams from eight source studies, leave-one-out cross-validation

with every free coefficient refitted in each fold results in a mean V_{exp}/V_{pred} ratio of 1.007, a coefficient of variation of 9.3%, and an R^2 of 0.827. When complete source studies are withheld, the coefficient of variation is 12.5%. The proposed model was compared on identical data with the PCI-UHPC provision applied as published, the FHWA and AFGC provisions with tensile inputs estimated from the fiber properties and the compressive strength, and the standard SMCFT. The proposed model attains the lowest Demerit Points Classification penalty (12 versus 30 for the PCI-UHPC provision), the lowest coefficient of variation (8.9% versus 17.6%), and the highest coefficient of determination. The model uncertainty follows a lognormal distribution with a bias factor $\lambda_R = 1.007$ and a model coefficient of variation $V_\theta = 8.9\%$. A reliability calibration within the ACI 318 LRFD framework results in a resistance factor of $\phi^* = 0.776$ (95% confidence interval [0.741, 0.814]), supporting a preliminary resistance factor of $\phi = 0.70$ for building load combinations within the scope of the database. All subgroups with at least five specimens attain resistance factors from 0.717 to 0.802, above the recommended $\phi = 0.70$. The separable fiber contribution, calculated from the model equations, averages 20.3% of the sectional capacity but spans from 10.8% to 23.2% across the ψ_f bins. The proposed model is applicable to non-prestressed UHPC beams with rectangular and I-sections containing both steel fibers and stirrups, within the ranges of the database, namely $2.0 \le a/d \le 4.0$, $1.0\% \le \rho_f \le 5.0\%$, $250 \le h \le 500$ mm, $3.6\% \le \rho_l \le 12.8\%$, and $114.5 \le f'_c \le 185.2$ MPa.

Future research should evaluate the proposed model on prestressed UHPC members, calibrate the resistance factor with the AASHTO LRFD load model, and test T-sections, deeper sections, and companion specimens differing only in fiber content.

Funding: This study was conducted without external funding.

Data Availability Statement: The data presented in this study were obtained from the supplementary material of Sapkota et al. [39] at https://doi.org/10.1038/s41598-025-13444-y.

Conflicts of Interest: The author declares no conflicts of interest.

References

1. Wille, K.; El-Tawil, S.; Naaman, A.E. Properties of strain hardening ultra high performance fiber reinforced concrete (UHP-FRC) under direct tensile loading. *Cem. Concr. Compos.* **2014**, *48*, 53–66. [CrossRef]
2. Yoo, D.Y.; Banthia, N. Mechanical properties of ultra-high-performance fiber-reinforced concrete: A review. *Cem. Concr. Compos.* **2016**, *73*, 267–280. [CrossRef]
3. Zhou, M.; Lu, W.; Song, J.; Lee, G.C. Application of Ultra-High Performance Concrete in bridge engineering. *Constr. Build. Mater.* **2018**, *186*, 1256–1267. [CrossRef]
4. Shaikh, F.U.A.; Luhar, S.; Arel, H.Ş.; Luhar, I. Performance evaluation of Ultrahigh performance fibre reinforced concrete—A review. *Constr. Build. Mater.* **2020**, *232*, 117152. [CrossRef]
5. Yoo, D.Y.; Banthia, N.; Yoon, Y.S. Recent development of innovative steel fibers for ultra-high-performance concrete (UHPC): A critical review. *Cem. Concr. Compos.* **2024**, *145*, 105359. [CrossRef]
6. Smarzewski, P. Mechanical properties and durability of ultra-high performance concrete containing steel fibers. *Compos. Struct.* **2025**, *371*, 119471. [CrossRef]
7. Sharma, R.; Jang, J.G.; Bansal, P.P. A comprehensive review on effects of mineral admixtures and fibers on engineering properties of ultra-high-performance concrete. *J. Build. Eng.* **2022**, *45*, 103314. [CrossRef]
8. Zheng, W.; Amin, M.N.; Khan, K.; Sufian, M.; Deifalla, A.F. A scientometric review of the literature on the incorporation of steel fibers in ultra-high-performance concrete with research mapping knowledge. *Rev. Adv. Mater. Sci.* **2023**, *62*, 20220310. [CrossRef]
9. Sritharan, S.; Doiron, G.; Bierwagen, D.; Keierleber, B.; Abu-Hawash, A. First Application of UHPC Bridge Deck Overlay in North America. *Transp. Res. Rec. J. Transp. Res. Board* **2018**, *2672*, 40–47. [CrossRef]
10. Lu, K.; Xu, Q.; Li, W.; Hu, Y.; Wang, J.; Yao, Y. Fatigue performance of UHPC bridge deck system with field-cast dovetail joint. *Eng. Struct.* **2021**, *237*, 112108. [CrossRef]
11. Shin, H.O.; Min, K.H.; Mitchell, D. Confinement of ultra-high-performance fiber reinforced concrete columns. *Compos. Struct.* **2017**, *176*, 124–142. [CrossRef]

12. Aboukifa, M.; Moustafa, M.A. Experimental seismic behavior of ultra-high performance concrete columns with high strength steel reinforcement. *Eng. Struct.* **2021**, *232*, 111885. [CrossRef]
13. Aboukifa, M.; Moustafa, M.A. Structural and buckling behavior of full-scale slender UHPC columns. *Eng. Struct.* **2022**, *255*, 113928. [CrossRef]
14. Naeimi, N.; Moustafa, M.A. Numerical modeling and design sensitivity of structural and seismic behavior of UHPC bridge piers. *Eng. Struct.* **2020**, *219*, 110792. [CrossRef]
15. Wakjira, T.G.; Alam, M.S. Performance-based seismic design of Ultra-High-Performance Concrete (UHPC) bridge columns with design example—Powered by explainable machine learning model. *Eng. Struct.* **2024**, *314*, 118346. [CrossRef]
16. Wakjira, T.G.; Alam, M.S. Hybrid machine learning-enabled multivariate bridge-specific seismic vulnerability and resilience assessment of UHPC bridges. *Resilient Cities Struct.* **2025**, *4*, 92–102. [CrossRef]
17. Kulkarni, A.; Shafei, B.; Epackachi, S. Structural response assessment of ultra-high performance concrete shear walls under cyclic lateral loads. *Struct. Concr.* **2023**, *24*, 2699–2720. [CrossRef]
18. Wang, X.; Huang, D.; Gao, Y.; Li, L. Experimental study on seismic performance of low strength shear walls strengthened with modified reactive powder concrete. *Structures* **2023**, *57*, 105094. [CrossRef]
19. Hong, S.G.; Lee, J.H.; Choi, Y.; Gu, I.Y. Seismic Strengthening of Concrete Columns by Ultrahigh-Performance Fiber-Reinforced Concrete Jacketing. *J. Struct. Eng.* **2021**, *147*, 04021157. [CrossRef]
20. Hou, C.; Ma, G.; Hwang, H.J.; Li, S.; Kang, S.M. Seismic retrofit of intact and damaged RC columns using prefabricated steel cage-reinforced UHPC jackets and NSM GFRP bars. *Eng. Struct.* **2024**, *317*, 118665. [CrossRef]
21. Wu, C.; Ma, G.; Zhu, D.; Qu, H.; Zhuang, H. Seismic retrofitting of GFRP-reinforced concrete columns using precast UHPC plates. *Soil Dyn. Earthq. Eng.* **2024**, *187*, 109024. [CrossRef]
22. Du, J.; Meng, W.; Khayat, K.H.; Bao, Y.; Guo, P.; Lyu, Z.; Abu-Obeidah, A.; Nassif, H.; Wang, H. New development of ultra-high-performance concrete (UHPC). *Compos. Part B Eng.* **2021**, *224*, 109220. [CrossRef]
23. Gong, J.; Ma, Y.; Fu, J.; Hu, J.; Ouyang, X.; Zhang, Z.; Wang, H. Utilization of fibers in ultra-high performance concrete: A review. *Compos. Part B Eng.* **2022**, *241*, 109995. [CrossRef]
24. Wu, Z.; Shi, C.; He, W.; Wu, L. Effects of steel fiber content and shape on mechanical properties of ultra high performance concrete. *Constr. Build. Mater.* **2016**, *103*, 8–14. [CrossRef]
25. Yoo, D.Y.; Lee, J.H.; Yoon, Y.S. Effect of fiber content on mechanical and fracture properties of ultra high performance fiber reinforced cementitious composites. *Compos. Struct.* **2013**, *106*, 742–753. [CrossRef]
26. Wille, K.; Naaman, A.E. Pullout Behavior of High-Strength Steel Fibers Embedded in Ultra-High-Performance Concrete. *ACI Mater. J.* **2012**, *109*, 479–488. [CrossRef]
27. Minelli, F.; Plizzari, G.A. On the Effectiveness of Steel Fibers as Shear Reinforcement. *ACI Struct. J.* **2013**, *110*, 379–390. [CrossRef]
28. Pekgökgöz, R.K.; Avcil, F. Effect of steel fibres on reinforced concrete beam-column joints under reversed cyclic loading. *J. Croat. Assoc. Civ. Eng.* **2021**, *73*, 1185–1194. [CrossRef]
29. Pourbaba, M.; Joghataie, A.; Mirmiran, A. Shear behavior of ultra-high performance concrete. *Constr. Build. Mater.* **2018**, *183*, 554–564. [CrossRef]
30. Lim, W.Y.; Hong, S.G. Shear Tests for Ultra-High Performance Fiber Reinforced Concrete (UHPFRC) Beams with Shear Reinforcement. *Int. J. Concr. Struct. Mater.* **2016**, *10*, 177–188. [CrossRef]
31. Zagon, R.; Matthys, S.; Kiss, Z. Shear behaviour of SFR-UHPC I-shaped beams. *Constr. Build. Mater.* **2016**, *124*, 258–268. [CrossRef]
32. Bermudez, M.; Hung, C.C. Shear Strength Equation and Database for High-Strength High-Performance Fiber-Reinforced Concrete and Ultra-High-Performance Concrete Beams without Stirrups. *ACI Struct. J.* **2024**, *121*, 185–195. [CrossRef]
33. Zerfu, K.; Fujiyama, C.; Maekawa, K.; Ichinomiya, T.; Kosaka, T. Shear transfer model for ultra-high-performance concrete incorporating fiber bridging mechanism. *Struct. Concr.* **2025**, *26*, 5999–6018. [CrossRef]
34. Baby, F.; Marchand, P.; Toutlemonde, F. Shear Behavior of Ultrahigh Performance Fiber-Reinforced Concrete Beams. I: Experimental Investigation. *J. Struct. Eng.* **2014**, *140*, 04013111. [CrossRef]
35. Voo, Y.L.; Poon, W.K.; Foster, S.J. Shear Strength of Steel Fiber-Reinforced Ultrahigh-Performance Concrete Beams without Stirrups. *J. Struct. Eng.* **2010**, *136*, 1393–1400. [CrossRef]
36. Yavaş, A.; Hasgul, U.; Turker, K.; Birol, T. Effective fiber type investigation on the shear behavior of ultrahigh-performance fiber-reinforced concrete beams. *Adv. Struct. Eng.* **2019**, *22*, 1591–1605. [CrossRef]
37. Sun, B.; Luo, R.; Quan, C.; Song, C.; Xiao, R. Shear behavior of prestressed UHPC rectangular beams: Experimental investigation and limit equilibrium state-based prediction method. *Arch. Civ. Mech. Eng.* **2024**, *24*, 31. [CrossRef]
38. Ye, M.; Li, L.; Yoo, D.Y.; Li, H.; Zhou, C.; Shao, X. Prediction of shear strength in UHPC beams using machine learning-based models and SHAP interpretation. *Constr. Build. Mater.* **2023**, *408*, 133752. [CrossRef]
39. Sapkota, S.C.; Shrestha, A.; Haq, M.; Paudel, S.; Tang, W.; Kamyab, H.; Rocchio, D. Enhancing shear strength predictions of UHPC beams through hybrid machine learning approaches. *Sci. Rep.* **2025**, *15*, 28259. [CrossRef]

40. El-Helou, R.G.; Graybeal, B.A. Shear Design of Strain-Hardening Fiber-Reinforced Concrete Beams. *J. Struct. Eng.* **2023**, *149*, 04022234. [CrossRef]
41. Graybeal, B.A.; Helou, R.G. *Structural Design with Ultra-High Performance Concrete*; Technical Report FHWA-HRT-23-077; Federal Highway Administration: McLean, VA, USA, 2023.
42. Solhmirzaei, R.; Salehi, H.; Kodur, V.; Naser, M.Z. Machine learning framework for predicting failure mode and shear capacity of ultra high performance concrete beams. *Eng. Struct.* **2020**, *224*, 111221. [CrossRef]
43. Ergen, F.; Katlav, M. Estimation of the shear strength of UHPC beams via interpretable deep learning models: Comparison of different optimization techniques. *Mater. Today Commun.* **2024**, *40*, 109394. [CrossRef]
44. Vecchio, F.J.; Collins, M.P. The Modified Compression-Field Theory for Reinforced Concrete Elements Subjected to Shear. *ACI J. Proc.* **1986**, *83*, 219–231. [CrossRef]
45. Bentz, E.C.; Vecchio, F.J.; Collins, M.P. Simplified Modified Compression Field Theory for Calculating Shear Strength of Reinforced Concrete Elements. *ACI Struct. J.* **2006**, *103*, 614–624. [CrossRef]
46. *CSA A23.3:19*; Design of Concrete Structures. Canadian Standards Association: Toronto, ON, Canada, 2019.
47. Bentz, E.C.; Collins, M.P. Development of the 2004 Canadian Standards Association (CSA) A23.3 shear provisions for reinforced concrete. *Can. J. Civ. Eng.* **2006**, *33*, 521–534. [CrossRef]
48. Wakjira, T.G.; Ebead, U. A shear design model for RC beams strengthened with fabric reinforced cementitious matrix. *Eng. Struct.* **2019**, *200*, 109698. [CrossRef]
49. Wakjira, T.; Ebead, U. Simplified Compression Field Theory-Based Model for Shear Strength of Fabric-Reinforced Cementitious Matrix-Strengthened Reinforced Concrete Beams. *ACI Struct. J.* **2020**, *117*, 91–104. [CrossRef]
50. Liu, T.; Charron, J.P. Analytical Model for Calculating Shear Capacity of NSC Beams Strengthened by UHPC Lateral Layers. *J. Struct. Eng.* **2024**, *150*, 04024049. [CrossRef]
51. Diab, A.; Ferche, A. Shear strength model for UHPC members incorporating fiber orientation and cross-sectional shape effects: Model formulation and database evaluation. *Eng. Struct.* **2025**, *327*, 119654. [CrossRef]
52. Tadros, M.K.; Lawler, J.; El-Khier, M.A.; Gee, D.; Kurt, A.; Lucier, G.; Wagner, E. *Implementation of Ultra-High Performance Concrete in Long-Span Precast Pretensioned Elements for Concrete Buildings and Bridges (Phase II Report)*; Technical Report; Precast/Prestressed Concrete Institute: Chicago, IL, USA, 2021. [CrossRef]
53. *ACI 318-19*; Building Code Requirements for Structural Concrete (ACI 318-19) and Commentary (ACI 318R-19). American Concrete Institute: Farmington Hills, MI, USA, 2019. [CrossRef]
54. Collins, M.P.; Mitchell, D.; Adebar, P.; Vecchio, F.J. A General Shear Design Method. *ACI Struct. J.* **1996**, *93*, 36–45. [CrossRef]
55. Li, V.C. Postcrack Scaling Relations for Fiber Reinforced Cementitious Composites. *J. Mater. Civ. Eng.* **1992**, *4*, 41–57. [CrossRef]
56. Naaman, A.E. Engineered Steel Fibers with Optimal Properties for Reinforcement of Cement Composites. *J. Adv. Concr. Technol.* **2003**, *1*, 241–252. [CrossRef]
57. Mészöly, T.; Randl, N. Assessment of Methods to Derive Tensile Properties of Ultra-High-Performance Fiber-Reinforced Cementitious Composites. *Materials* **2024**, *17*, 3259. [CrossRef]
58. Lee, S.C.; Cho, J.Y.; Vecchio, F.J. Simplified Diverse Embedment Model for Steel Fiber-Reinforced Concrete Elements in Tension. *ACI Mater. J.* **2013**, *110*, 403–412. [CrossRef]
59. Lee, S.C.; Cho, J.Y.; Vecchio, F.J. Diverse Embedment Model for Steel Fiber-Reinforced Concrete in Tension: Model Development. *ACI Mater. J.* **2011**, *108*, 516–525. [CrossRef]
60. AFGC. *Ultra High Performance Fibre-Reinforced Concretes: Recommendations*, revised ed.; Association Française de Génie Civil: Paris, France, 2013.
61. *NF P 18-710*; National Addition to Eurocode 2—Design of Concrete Structures: Specific Rules for Ultra-High Performance Fibre-Reinforced Concrete (UHPFRC). Association Française de Normalisation (AFNOR): La Plaine Saint-Denis, France, 2016.
62. Graybeal, B.A. *Material Property Characterization of Ultra-High Performance Concrete*; Technical Report FHWA-HRT-06-103; Federal Highway Administration: McLean, VA, USA, 2006.
63. Zsutty, T. Shear Strength Prediction for Separate Categories of Simple Beam Tests. *ACI J. Proc.* **1971**, *68*, 138–143. [CrossRef]
64. Moraes Neto, B.N.; Barros, J.A.O.; Melo, G.S.S.A. Model to Simulate the Contribution of Fiber Reinforcement for the Punching Resistance of RC Slabs. *J. Mater. Civ. Eng.* **2014**, *26*, 04014020. [CrossRef]
65. Cao, X.; He, D.; Qian, K.; Fu, F.; Deng, X.F.; Wang, L. Shear behavior of glass FRP bars-reinforced ultra-high performance concrete I-shaped beams. *Struct. Concr.* **2023**, *24*, 1503–1520. [CrossRef]
66. Zhou, L.; Wan, S. Shear behavior of UHPC beams with small shear span to depth ratios based on MSTM. *Case Stud. Constr. Mater.* **2022**, *16*, e01134. [CrossRef]
67. Cao, X.; Deng, X.F.; Jin, L.Z.; Fu, F.; Qian, K. Shear capacity of reactive powder concrete beams using high-strength steel reinforcement. *Proc. Inst. Civ. Eng.-Struct. Build.* **2021**, *174*, 276–291. [CrossRef]
68. Ma, K.Z.; Ma, Y.D.; Xing, G.H.; Liu, B.Q. Study on shear behavior of reinforced ultra-high performance concrete beams. *J. Build. Struct.* **2022**, *43*, 179–188. (In Chinese) [CrossRef]

69. Jin, L.Z.; Li, Y.X.; Qi, K.N.; He, P. Research on shear bearing capacity and ductility of high strength reinforced RPC beam. *Eng. Mech.* **2015**, *32*, 209–214, 225. (In Chinese) [CrossRef]
70. Liang, X.W.; Wang, Z.Y.; Yu, J.; Li, L. Study on shear behavior and shear bearing capacity of UHPC beams with stirrups. *China Civ. Eng. J.* **2018**, *51*, 56–67. (In Chinese) [CrossRef]
71. Mészöly, T.; Randl, N. Shear behavior of fiber-reinforced ultra-high performance concrete beams. *Eng. Struct.* **2018**, *168*, 119–127. [CrossRef]
72. Ji, W.; Li, W.; An, M.; Zhu, L. Shear Capacity of T-Section Girders Made of Reactive Powder Concrete. *J. Bridge Eng.* **2018**, *23*, 04018041. [CrossRef]
73. Lu, Z.F.; Tong, L.P.; Liu, M.Y.; Zhang, Q.; Wang, J. Experimental study on shear performance of lightweight ultra-high performance concrete beam. *J. Wuhan Univ. Technol.* **2021**, *43*, 50–56. (In Chinese)
74. Minelli, F.; Vecchio, F.J. Compression Field Modeling of Fiber-Reinforced Concrete Members Under Shear Loading. *ACI Struct. J.* **2006**, *103*, 244–252. [CrossRef]
75. Kwak, Y.K.; Eberhard, M.O.; Kim, W.S.; Kim, J. Shear Strength of Steel Fiber-Reinforced Concrete Beams without Stirrups. *ACI Struct. J.* **2002**, *99*, 530–538. [CrossRef]
76. Tarawneh, A.; Amirah, H.; Alghossoon, A.; Almasabha, G.; Al-Mazaidh, R.; Saleh, E. Performance Evaluation of Current Design Models in Predicting Shear Resistance of UHPC Girders. *J. Compos. Sci.* **2025**, *9*, 211. [CrossRef]
77. Nowak, A.S.; Szerszen, M.M. Calibration of Design Code for Buildings (ACI 318): Part 1—Statistical Models for Resistance. *ACI Struct. J.* **2003**, *100*, 377–382. [CrossRef]
78. Nowak, A.S.; Rakoczy, A.M. Uncertainties in the Building Process. *Bull. Pol. Acad. Sci. Tech. Sci.* **2013**, *61*, 129–135. [CrossRef]
79. Poudel, B.; Kalmogo, P.; Aaleti, S. Statistical Evaluation and Reliability Analysis of Interface Shear Capacity in Ultra-High-Performance Concrete Members. *Buildings* **2024**, *14*, 3064. [CrossRef]
80. Szerszen, M.M.; Nowak, A.S. Calibration of Design Code for Buildings (ACI 318): Part 2—Reliability Analysis and Resistance Factors. *ACI Struct. J.* **2003**, *100*, 383–391. [CrossRef]
81. Milutinovic, G.; Hajdin, R. Dependence of Sensitivity Factors on Ratio of Traffic Load to Dead Load. *Appl. Sci.* **2024**, *14*, 985. [CrossRef]
82. AASHTO. *AASHTO LRFD Bridge Design Specifications*, 9th ed.; American Association of State Highway and Transportation Officials: Washington, DC, USA, 2020.

Disclaimer/Publisher's Note: The statements, opinions and data contained in all publications are solely those of the individual author(s) and contributor(s) and not of MDPI and/or the editor(s). MDPI and/or the editor(s) disclaim responsibility for any injury to people or property resulting from any ideas, methods, instructions or products referred to in the content.